nature neuroscience

Article

https://doi.org/10.1038/s41593-023-01347-y

Cerebellar associative learning underlies skilled reach adaptation

Received: 17 December 2021

Accepted: 24 April 2023

Dylan J. Calame[1,2], **Matthew I. Becker**[1,2] & **Abigail L. Person**[3]

The cerebellum is hypothesized to refine movement through online adjustments. We examined how such predictive control may be generated using a mouse reach paradigm, testing whether the cerebellum uses within-reach information as a predictor to adjust reach kinematics. We first identified a population-level response in Purkinje cells that scales inversely with reach velocity, pointing to the cerebellar cortex as a potential site linking kinematic predictors and anticipatory control. Next, we showed that mice can learn to compensate for a predictable reach perturbation caused by repeated, closed-loop optogenetic stimulation of pontocerebellar mossy fiber inputs. Both neural and behavioral readouts showed adaptation to position-locked mossy fiber perturbations and exhibited aftereffects when stimulation was removed. Surprisingly, position-randomized stimulation schedules drove partial adaptation but no opposing aftereffects. A model that recapitulated these findings suggests that the cerebellum may decipher cause-and-effect relationships through time-dependent generalization mechanisms.

Cerebellar damage and disease lead to motor abnormalities such as discoordination, dysmetric movement endpoints and the inability to adapt movements to new conditions[1–6]. This array of symptoms suggests that the cerebellum may improve motor control by learning anticipatory control signals, such as those that mediate predictive control[7–10]. Cerebellar learning paradigms, such as classical conditioning and motor adaptation, have provided clues into the neurobiological basis of these learned anticipatory signals[11]. Delay eyeblink conditioning, for example, illustrates how neutral conditioned stimuli paired with reflex-eliciting unconditioned stimuli become predictive cues eliciting conditioned responses (for example, a tone repeatedly paired with a corneal air puff eventually elicits a predictive eyeblink). Mechanistically, neutral cues can be replaced fully by cerebellar mossy fiber stimulation[12,13] and unconditioned stimuli can be replaced fully by climbing fiber stimulation[13]. Climbing fibers elicit complex spikes (Cspks) in Purkinje cell (PC) dendrites[14,15] that, over many trials, reduce parallel fiber efficacy onto PCs, leading to firing rate pauses at the predicted time of the unconditioned stimulus. Through subsequent disinhibition of the cerebellar nuclei, these pauses then drive anticipatory conditioned responses. Similar mechanisms are proposed to underlie motor adaptation, where adaptive changes to behavior, which are consistently associated with instructive Cspks, are attributed to reweighting of sensorimotor information conveyed to the cerebellum[16–19].

Key differences, however, between motor adaptation and classical conditioning raise important questions about sites of learning. For example, skilled movements, such as reach, involve both cerebral cortex and cerebellum, both of which may change with adaptation[20–23]. Thus, learning-related changes in cerebellar Purkinje firing could be inherited from the cerebral cortex, generated by cerebellar plasticity or both[24]. More generally, perturbations that drive motor adaptation[22,25,26,27] engage sensorimotor feedback loops at multiple levels of the nervous system. This complicates the view that cerebellar input–output remapping explains adaptation fully because inconsistent cerebellar inputs, caused by learning at sites outside the cerebellum, would deprive associative mechanisms of a stable cue.

Here, we leveraged a recent discovery that acute disruption of cerebral cortical input to the cerebellum impairs skilled reach kinematics[28]. We reasoned that, because mossy fiber stimulation can be used as an associative cue in delay eyelid conditioning and is hypothesized to be remapped in motor adaptation, we could explicitly link these roles by

---

[1]Neuroscience Graduate Program, University of Colorado School of Medicine, Aurora, CO, USA. [2]Medical Scientist Training Program, University of Colorado School of Medicine, Aurora, CO, USA. [3]Department of Physiology and Biophysics, University of Colorado School of Medicine, Aurora, CO, USA. e-mail: abigail.person@cuanschutz.edu

using optogenetic activation of cerebellar inputs to both perturb and predictively cue skilled reach adjustments. We monitored kinematic and neurophysiological signatures of learning while applying repeated optogenetic manipulations of mossy fibers in closed loop with reach, triggered at either consistent or randomized kinematic landmarks. A cerebellar model of timed adaptation within a movement recapitulated our key experimental findings and gives mechanistic insight into the circuit properties underlying cerebellar reach adaptation. Together, these experiments unify the frameworks of cerebellar associative learning and motor adaptation in skilled movements, an important step in understanding mechanisms of motor learning and predictive control.

Results

A PC population code tuned to reach velocity

Neurons in the anterior interposed nucleus fire proportionally to reach velocity and scale limb deceleration causally, such that the limb lands on target despite initial kinematic variability[2,29]. To determine whether upstream PCs may drive these decelerative bursts in the cerebellar nuclei, we combined kinematic and electrophysiological recordings in mice engaged in a skilled, head-fixed reach task. After mice were proficient at the task, we recorded reach kinematics with high-speed cameras via an infrared-reflective marker affixed to the mouse's hand (Fig. 1a and Extended Data Fig. 1). Acute recordings in the cerebellar cortex were made simultaneously, using either single electrodes or Neuropixel probes (Fig. 1a and Supplementary Video 1). Recordings were targeted to a cerebellar cortical site situated between lobules 4 and 5 and the lobule simplex known to influence forelimb movements in mice[11]. Confirmed PCs were identified by the presence of Cspks and an associated simple spike pause, whereas putative PCs were identified as neurons with a firing rate of >40 spikes s^{-1}, coefficient of variation 2 (CV2) of >0.20 and median absolute difference from the median interspike interval (MAD) of <0.008 (Methods; Extended Data Fig. 2). For many of the analyses below, we pooled confirmed and putative PCs, and refer to them simply as PCs, because simple spike statistics are unique to PCs relative to all other known cerebellar cortical cell types. We note the caveat that future studies may uncover new cell types that are inadvertently included in our analyses. Therefore, supplemental data restricted to confirmed PCs are also provided for select analyses.

We found that activity in many PCs was highly modulated around the time of the reach across cells and sessions (Fig. 1). To test the prediction that decelerative signals in the cerebellar nuclei derive from Purkinje neuron activity patterns during reach, we first sought to understand what individual PCs encode. We used least absolute shrinkage and selection operator (LASSO) regression to model PC simple spike firing rate using limb kinematics on a trial-by-trial basis, with a tenfold crossvalidation step to avoid overfitting (Fig. 1b; Methods)[30]. On average, kinematics of the limb alone could explain a modest 18.0 ± 0.01% (mean ± standard error of the mean) of the variance in simple spike firing rate on individual trials, although trial-averaged data was a much closer fit (58.0 ± 0.01%; Fig. 1c,d), consistent with other studies of PC simple spike tuning to limb movements in primates[31–35]. Kinematic encoding was not a result of generic movement-related modulation but was specific to the kinematics of individual reaches, as demonstrated by two control analyses: first, a 'reach-shuffled' control reassigned PC firing to different reaches; and, second, a 'spike-shuffled' control, where simple spike times on each trial were time shuffled and regressed against kinematics. In both cases, regression performance on the empirical data was significantly higher than the shuffled controls, indicating simple spike firing rates encode reach kinematics on a reach-by-reach basis (Fig. 1d; $N = 11$ animals, $n = 465$ cells; for empirical versus reach shuffle, $P = 1.1 \times 10^{-71}$, weights (W) = 103,803, correlation coefficient (r) = 0.83; for empirical versus spike shuffle, $P = 6.9 \times 10^{-78}$, $W = 108{,}331$, $r = 0.87$; Wilcoxon signed-rank test). The regression model performance was stable across the spatial trajectory of reaches, suggesting kinematic encoding is continuous in individual cells (Fig. 1e). Comparable values were seen in Cspk-identified PCs (Extended Data Fig. 3f,g; $N = 8$ animals, $n = 59$ cells; for empirical versus reach shuffle, $P = 4.4 \times 10^{-11}$, $W = 1{,}758$, $r = 0.86$; for empirical versus spike shuffle, $P = 2.4 \times 10^{-11}$, $W = 1{,}770$, $r = 0.87$; Wilcoxon signed-rank test). To assess which kinematic variables in the regression model were the most important in modeling simple spike firing rate, we repeated the regression with each variable independently time shuffled and measured the change in variance explained relative to the complete model[36] (Extended Data Fig. 3d,e,h,i). Positional terms—outward, upward and lateral—each accounted for approximately 10% of the explained variance of the complete model, with each of the remaining 20 variables accounting for <5%, although there was a wide variety in the relative importance of different kinematic variables across cells. These measurements are roughly consistent with PC–limb kinematic relationships observed in primates[24,34]; however, the relatively weak encoding on individual trials obscures how the cerebellum might influence control over movements to make them smooth and accurate.

As noted previously, PC simple spike rates fluctuate during movements, with modulations that are either predominately positive or negative[37,38]. Of 465 PCs recorded during reach, 226 displayed increases in activity during the reach epoch and 239 showed a decrease (Fig. 1f). When segregated into groups that predominantly increase or decrease rates during reach, both populations had lower firing rates during faster

Fig. 1 | Net population activity in PCs predicts reach velocity. a, Schematic diagram of conceptual framework and experimental paradigm. Predictions computed by the cerebellum are hypothesized to be learned through reweighting of cerebellar inputs, including copies of motor commands, instructed by changes in climbing fiber activity. PCs of the deep central sulcus were recorded with either single electrodes or Neuropixel probes while the reaching hand was tracked in real time with high-speed cameras. **b**, Kinematic regressors in multilinear LASSO regression were used to model firing rates on individual reaches across sessions. **c**, Examples of three PCs fit with LASSO regression. Top, trial-averaged empirical and LASSO-predicted firing rates. Bottom, outward position and velocity aligned to firing rate at optimal lag. **d**, Modest single-trial R^2 for single cells in empirical, reach-shuffled and spike-shuffled LASSO regressions. $P = 1.1 \times 10^{-71}$ for empirical versus reach shuffle, $P = 6.9 \times 10^{-78}$ for empirical versus spike shuffle; Wilcoxon signed-rank test. **e**, Absolute model error (empirical versus predicted, across outward, upward and lateral positions) as a function of reach position. Stable error suggests continuous encoding of reach kinematics across reach epoch. Positions binned at 0.1 cm. **f**, During reach (kinematics, green), PCs group roughly into cells that increase firing rate (red) and cells that decrease firing rate (blue), aligned to the time the hand passed the 'threshold', 1 cm in the outward direction. **g**, Simple spike firing rate modulation during reaches grouped by reach speed. Cells that increase (red) and decrease (blue) firing rate both showed lower firing rates during faster reaches. Dashed lines represent time of peak rate modulation. **h**, Pooling all PCs reveals net firing rate suppression that scales with reach velocity percentile. Top, binned reach velocities associated with recordings. Bottom, net PC population firing rate change for each reach velocity bin. **i**, Magnitude of net firing rate suppression in total PC population as a function of outward velocity. Firing rate during the suppression in population activity was strongly negatively related to reach velocity. $P = 4.0 \times 10^{-4}$; linear regression. **j**, Time of population suppression is intermediate between peak outward acceleration and peak outward velocity, preceding deceleration. Plot relates the median timing of reach start, peak outward acceleration, peak outward velocity and peak outward deceleration to the time of population simple spike suppression for each reach velocity bin shown in **i**. Sample size: $N = 11$ animals, $n = 465$ cells. $^*P < 0.05$. All error bars and bands represent mean ± s.e.m. In box-and-whisker plots, box denotes median and 25th–75th percentiles, whiskers denote 10th and 90th percentiles; circle indicates mean. CbN, cerebellar nuclei; CS, complex spike; IO, inferior olive; MF, mossy fibers; SS, simple spike; FR, firing rate; max, maximum; pos., position; s.e.m., standard error of the mean; Sspk, simple spike; vel., velocity.

reaches relative to slower reaches (Fig. 1g; highest peak velocity). The peak rates of the population of positively modulated cells preceded negatively modulated cells (dashed vertical lines, ~220 ms difference), raising the question of how these subpopulations collaborate as a group.

Populations of ~40 PCs converge onto single nuclear cells[39]. In the oculomotor vermis—where heterogenous rate modulation profiles of PCs strongly resemble the patterns we saw during reach—grouping PCs into populations across classes revealed much stronger

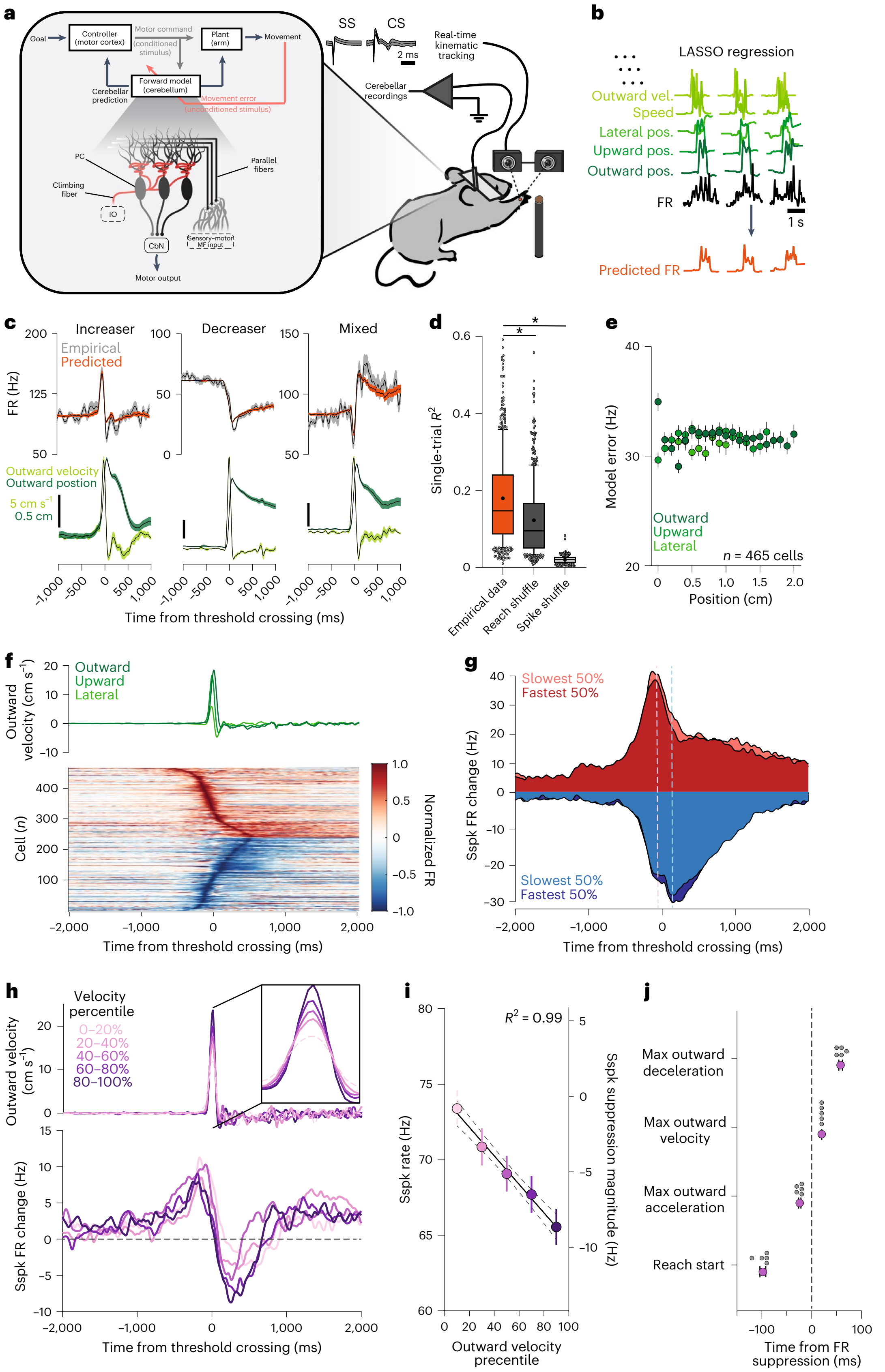

kinematic relationships with saccades[37,40]. Speculating that similar population-encoding principles may be seen in reach-related PCs, we next grouped all PCs across all animals and looked at average activity for reaches binned by outward velocity. Firing rate increases were followed by sharp drops in net activity during the reach epoch that scaled with the velocity of outreach (Fig. 1h). Quantifying the minimum simple spike firing rate during the reach window (Methods) showed a strong negative relationship with outreach velocity, such that the population showed a suppression of activity that scaled with reach velocity (Fig. 1i; $N = 11$ animals, $n = 465$ cells, 2,100 reaches, 11,806 reach–cell pairs; coefficient of determination (R^2) = 0.99, slope = −0.094, with 95% confidence interval [−0.111, −0.077], $P = 4.0 \times 10^{-4}$, $F = 307.5$). This observation held in the Cspk-identified PC subpopulation, with significantly deeper rate modulation on faster reaches (Extended Data Fig. 3j,k; $N = 8$ animals, $n = 59$ cells, $n = 1{,}003$ reaches, 1,665 reach–cell pairs; $P = 3.7 \times 10^{-2}$, $W = 325{,}815$, $r = 0.068$; Wilcoxon signed-rank test). The timing of rate suppression was intermediate between peak outward acceleration and peak outward velocity, just before the transition to the decelerative phase of reach (Fig. 1j and Extended Data Fig. 3l). Notably, each velocity percentile contained equal populations of positively and negatively modulated neurons. These data suggest that PC suppression scales in a way that is the inverse of decelerative nuclear bursts that slow the limb causally.

In summary, we found that individual PCs are privately and modestly tuned to specific kinematic features of reach but weakly related to previously observed patterns of firing in the cerebellar nuclei. Yet, at the population level, PC activity shows scaled suppression in activity shortly before deceleration, consistent with a disinhibitory mechanism driving decelerative bursts in nuclear cells. We hypothesize that this firing rate suppression may be mechanistically akin to conditioned responses seen in delay eyeblink conditioning—learned rate changes that produce anticipatory movements in response to predictive cues. Both the precise timing and scaling of the population activity suppression observed here are consistent with learned cerebellar responses linked to motor and sensory contingencies to control movement. As such, this behavior offers a unique opportunity to test theories relating motor adaptation to associative learning in service of skilled movement[18,41–43].

Cspks signal movement onset and reach outcome

To probe mechanisms that might shape cerebellar cortex scaling of output as a function of kinematics, we first identified cerebellar recordings with Cspks, the drivers of learning in PCs. Cspks could be sorted stably across the experiment in 59 of 465 putative PCs, 58 of which had Cspks during the perireach window (~1-s window centered on reach; Methods). Cspk probability increased shortly before movement onset, consistent with reports of early synchronized Cspk activity occurring at movement initiation[44,45], then dropped near steady-state levels (Fig. 2a; $P = 3.3 \times 10^{-5}$, $F = 2.6$, repeated measures (RM) one-way analysis of variance (ANOVA); mean Cpsk probability versus −500-ms bin, $P = 7.1 \times 10^{-4}$, Cohen's d (d) = −0.62, Dunnett's multiple comparisons test). In addition, a wide literature relates late Cspks occurring after movement initiation to movement errors and sculpting of simple spike rates during movement. Therefore, we analyzed the kinematics of reaches with early or late Cspks (Methods). Trials with late Cspks had distinct kinematics compared with trials without late Cspks, showing significantly deviated endpoints (Fig. 2b–e, $N = 8$ animals, $n = 58$ cells; Euclidean distance from session median for no Cspk trials versus Cspk trials, $P = 8.1 \times 10^{-4}$, $W = -847$, $r = -0.43$, Wilcoxon signed-rank test) but not peak velocity (Fig. 2f; $P = 0.81$, $t = 0.24$, $d = 0.032$, paired t-test). By contrast, reaches with early Cspks had no discernable kinematic differences (Extended Data Fig. 4a,b; $N = 8$ animals, $n = 58$ cells; Euclidean distance from session median for no Cspk trials versus Cspk trials, $P = 0.32$, $W = -257$, $r = -0.13$, Wilcoxon signed-rank test; peak velocity for no Cspk trials versus Cspk trials, $P = 0.75$, $t = 0.32$, $d = -0.042$, paired t-test), although we cannot rule out changes in reaction time[45,46].

To test whether PC tuning is unique on Cspk trials, indicative of an encoding error, we compared simple spike rates on Cspk and non-Cspk trials for early and late Cspks. Across neurons, simple spike rate was significantly elevated on late-Cspk trials (Fig. 2g,h; no-Cspk trials versus Cspk trials, $P = 2.8 \times 10^{-4}$, $t = 3.9$, $d = -0.51$, paired t-test), and this elevation led to a shift in the relationship of simple spike rate to reach velocity (Fig. 2i; no-Cspk trials versus Cspk trials, $P = 1.0 \times 10^{-3}$, $W = -833$, $r = -0.42$, Wilcoxon signed-rank test). Trials with early Cspks did not show elevated simple spike rates during outreach or changes in the relationship between simple spikes and reach velocity across sessions (Extended Data Fig. 4c–e; simple spike rate during outreach, for no-Cspk trials versus Cspk trials, $P = 0.37$, $t = 0.90$, $d = -0.12$, paired t-test; simple spike rate to peak velocity ratio, for no-Cspk trials versus Cspk trials, $P = 0.29$, $W = -273$, $r = -0.14$, Wilcoxon signed-rank test). Cspks function to depress PC inputs, leading to reductions of simple spike rate. If Cspks are responding to erroneous simple spike elevation, we speculated that simple spike rate should be elevated shortly before the time of a Cspk, as has been previously demonstrated[47]. Therefore, we analyzed simple spike rates aligned to the time of the Cspk, or the same time on the previous or next trial. In late-Cspk trials, Cspks were associated with higher-than-average simple spike rates in the 100 ms before a Cspk compared with the previous trial, and simple spikes in this window were lowered on the trial after the Cspk trial (Fig. 2j,k; $P = 9.8 \times 10^{-4}$, $F = 8.0$, RM one-way ANOVA; for previous trial versus Cspk trial, $P = 3.6 \times 10^{-3}$, $d = -0.45$; for Cspk trial versus next trial, $P = 0.024$, $d = 0.36$; Tukey's multiple comparisons test). In contrast, early Cspks that occurred before the onset of reach did not display increases in simple spikes before the Cspk (Extended Data Fig. 4f,g; $P = 0.17$, $F = 0.69$, RM one-way ANOVA). Together, these data reveal dynamics of PC Cspks, simple spikes and associated kinematics that suggest a continuous recalibration of kinematic tuning in PCs.

Behavioral adaptation to mossy fiber stimulation

Next, we sought to probe whether PCs reweight cerebellar inputs that shape movement kinematics. Previous work has shown that stimulation of pontine afferents to the cerebellum perturbs reaching movements in mice[28]. This effect is interpretable as corrupted cortical information entering the cerebellum, which initially drives an erroneous cerebellar control policy observable in acute kinematic effects. If cerebellar associative learning mechanisms implement the formation of an anticipatory control policy, a number of predictions emerge: pontocerebellar mossy fiber stimulation that drives reach errors will, when repeated over many reaches, lead to adaptation of PC responsivity. Removing the perturbation should lead to aftereffects due to accumulated learning of new contingencies. Finally, adaptation and aftereffects will be dependent on the temporal context of the perturbation within the movement, where learning only accumulates when perturbations are temporally locked to the execution of the movement.

To drive erroneous activity in PCs during reaching movements, we injected AAV-expressing hSyn-ChR2 into the pontine nuclei in mice, a major hub relaying motor commands from motor cortex to the cerebellum[28,48,49] (Fig. 3 and Extended Data Figs. 5a and 6a,b). Recordings of PCs showed that optogenetic stimulation of mossy fiber afferents in the cerebellar cortex drove both increases and decreases in simple spike firing rates (Extended Data Fig. 5b; $N = 4$ animals; 43 of 151 cells, 26 increase, 17 decrease; $P < 0.05$, paired t-test). This diverging stimulation effect is likely due to network properties in the cerebellar input layers leading to either net excitatory or inhibitory drive onto PCs[28]. Interestingly, cells with sorted Cspks (Methods) showed a small but significant increase in Cspk probability in the 250 ms after stimulation during rest compared with the probability outside of this epoch in response to mossy fiber stimulation (Extended Data Fig. 5c; $N = 4$ animals; $n = 39$ cells; $P = 5.6 \times 10^{-3}$, $t = 2.9$, $d = -0.45$, paired t-test), consistent with previous findings during electrical stimulation of mossy fibers[50]. Cspks time locked to mossy fiber stimulation suggest that optogenetically driven simple spikes may engage plasticity mechanisms to respond to perturbation.

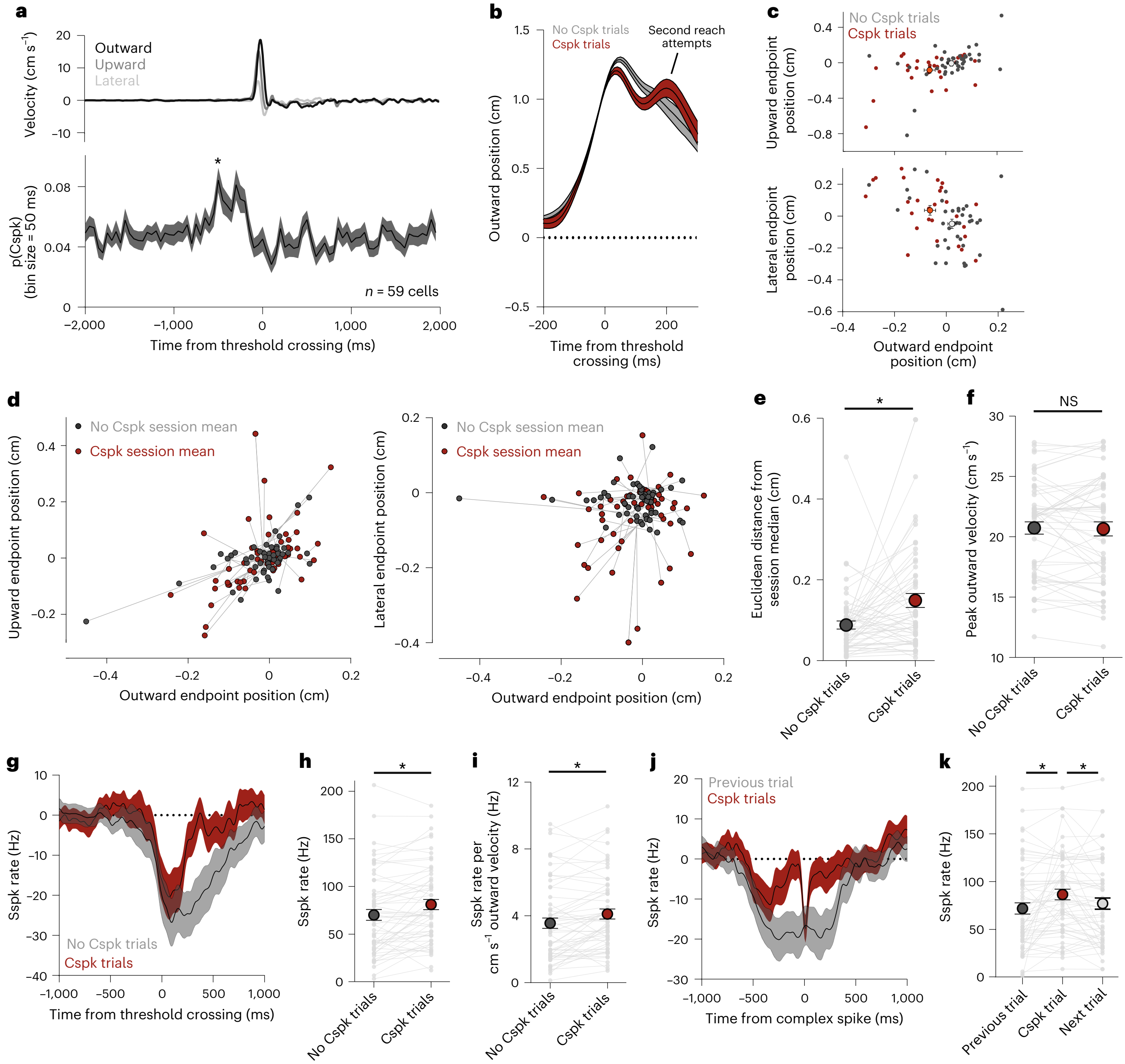

Fig. 2 | Reaches with Cspks have erroneous kinematics and elevated simple spike rates. a, Cspks are positively modulated in the 500 ms before reach before dropping close to baseline values. Top, mean velocity of reaches with Cspks recorded. Bottom, peri-event time histogram (PETH) of Cspk activity relative to the time of threshold crossing. $N = 8$ animals, $n = 59$ cells. $P = 3.3 \times 10^{-5}$, RM one-way ANOVA; $P = 7.1 \times 10^{-4}$, post hoc Dunnett's multiple comparisons test (*); p is probability in p(Cspk). **b**, Positional profiles from an example session separated into reaches with (red) and without Cspks (black) during or shortly after outreach. **c**, Endpoint of reaches relative to session median in the outward and upward directions (top) and outward and lateral directions (bottom) for trials with and without Cspks. Large red or gray dot indicates mean and s.e.m. from Cspk and non-Cspk reaches. For **b** and **c**, $N = 28$ Cspk reaches, 48 non-Cspk reaches. **d**, Session endpoints relative to session median for Cspk and non-Cspk reaches for each recorded cell with Cspks during or after outreach. Gray line links Cspk endpoint average with non-Cspk endpoint average for an individual session with the recorded cell. Left, outward and upward endpoint position. Right, outward and lateral endpoint position. **e**, Reach endpoints on Cspk trials were significantly further from session median compared with non-Cspk trials. $P = 8.1 \times 10^{-4}$, Wilcoxon signed-rank test. **f**, Peak outward velocity was not significantly different between Cspk and non-Cspk trials. $P = 0.81$, paired *t*-test. **g**, PC Sspks on Cspk and non-Cspk trials aligned to threshold crossing. **h**, PC Sspk rates were significantly higher during outreach in trials with Cspks. $P = 2.8 \times 10^{-4}$, paired t-test. **i**, Ratio of simple spike rate to outward velocity was significantly higher during outreach in trials with Cspks. $P = 1.0 \times 10^{-3}$, Wilcoxon signed-rank test. **j**, Simple spike rate aligned to the time of a Cspk, or simple spikes aligned to the same time relative to threshold crossing on the previous trial showed simple spike increases shortly before the Cspk. **k**, Quantification of simple spike rates in the 100 ms before a Cspk on a Cspk trial or the previous or next trial aligned to the same time of the Cspk relative to threshold crossing. $P = 9.8 \times 10^{-4}$, RM one-way ANOVA; for previous trial versus Cspk trial, $P = 3.6 \times 10^{-3}$; for Cspk trial versus next trial, $P = 0.024$; Tukey's multiple comparisons test. For **d**–**k**, $N = 8$ animals, $n = 58$ cells. $^*P < 0.05$. All error bars and bands represent mean ± s.e.m. In box-and-whisker plots, box denotes median and 25th–75th percentiles, whiskers denote 10th and 90th percentiles and circle indicates the mean. NS, not significant.

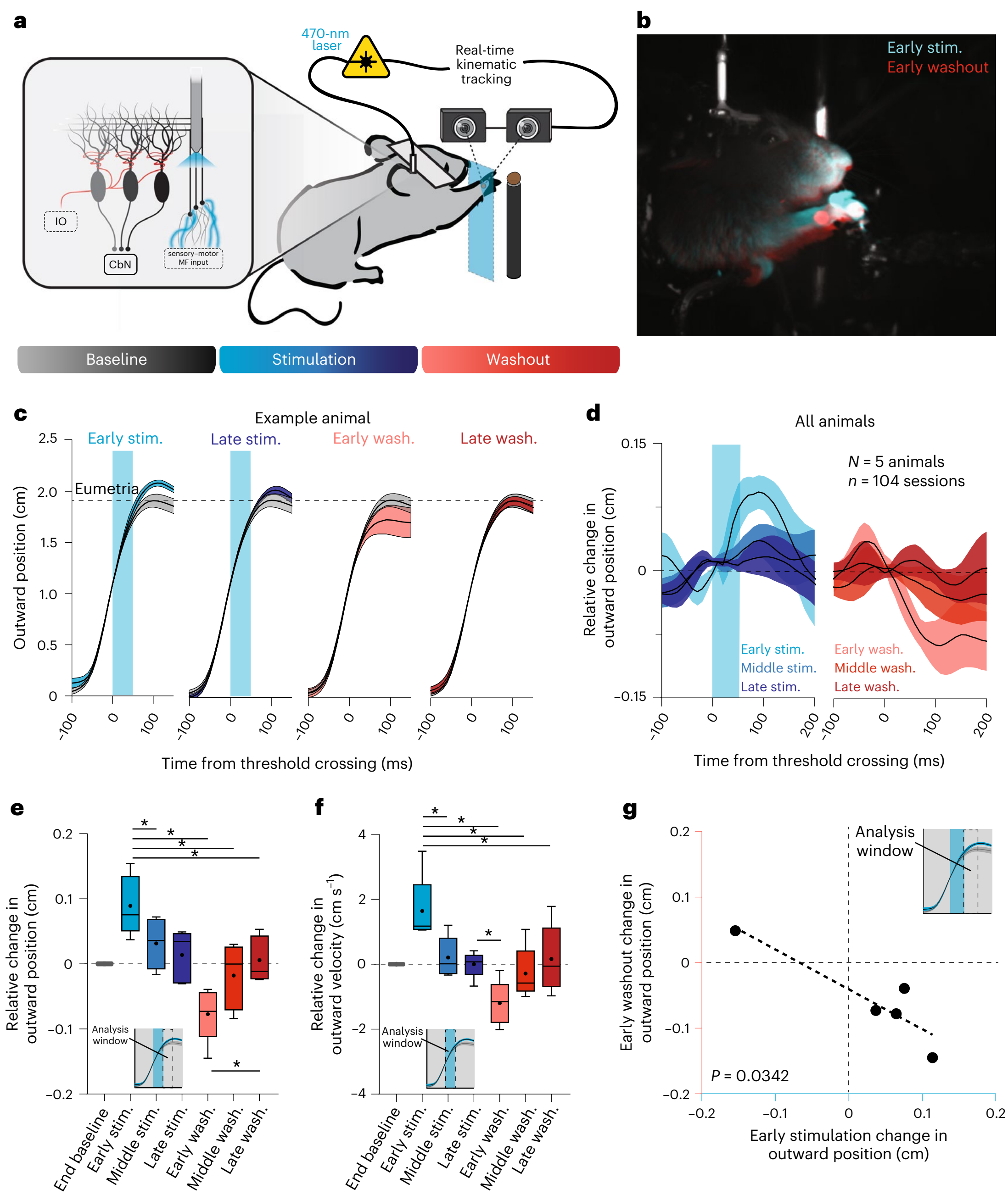

Fig. 3 | Adaptation to mossy fiber stimulation during reach. a, Head-fixed mice expressing ChR2 in pontocerebellar mossy fibers were trained to reach for food pellets while the hand was tracked with high-speed cameras. On laser trials, light directed to the cerebellar primary fissure through an implanted fiber was triggered in closed loop after the hand crossed a plane 1 cm outward from reach start position. Bottom, perturbation schedule followed canonical adaptation structure, with a baseline (no-stimulation) block, stimulation block with stimulation on every reach, followed by a washout block with stimulation omitted. **b**, Hand position 100 ms after threshold crossing in the first stimulated (blue) and washout (red) reaches heading to the target (white), after ref. 28. **c**, Hand position during baseline (gray), compared with hand position measured across the adaptation and washout blocks in an example mouse. Blue shading denotes the time of mossy fiber stimulation. *n* = 1 animal, 20 sessions. **d**, Summary of stimulation-induced kinematic effects, which decay over the adaptation block and show opposing aftereffects. Baseline subtracted hand position, rectified relative to the direction of kinematic effect of stimulation, is shown for reaches in the early (first reach), middle (middle five) and late (last five) phases for both stimulation (blue) and washout (red) blocks. **e**, Summary of adaptation effects across animals and sessions. Relative change in outward position was assessed in the 50-ms window after the end of stimulation. Asterisks indicate statistically significant differences between blocks. $P = 1.7 \times 10^{-3}$, RM one-way ANOVA; for early stimulation to middle stimulation, $P = 8.9 \times 10^{-3}$; for early stimulation to early washout, $P = 0.030$; for early stimulation to middle washout, $P = 0.017$; for early stimulation to late washout, $P = 0.031$; for early washout to late washout, $P = 0.042$; Tukey's multiple comparisons test. **f**, Same as **e**, but with outward velocity assessed in the 50 ms after the start of stimulation. $P = 4.7 \times 10^{-3}$, RM one-way ANOVA; for early stimulation to middle stimulation, $P = 0.024$; for early stimulation to early washout, $P = 0.041$; for early stimulation to middle washout, $P = 3.5 \times 10^{-3}$; for early stimulation to late washout, $P = 0.030$; for late stimulation to early washout, $P = 0.048$; Tukey's multiple comparisons test. **g**, The magnitude and direction of early stimulation effect was related to aftereffects. Plot shows linear regression relating the magnitude of the early stimulation outward position effect and early washout outward position effect compared with baseline reaches. $P = 0.034$, linear regression. For **d**–**g**, $N = 5$ mice, 104 sessions. *$P < 0.05$. All error bars and bands represent mean ± s.e.m. In box-and-whisker plots, box denotes median and 25th–75th percentiles, whiskers denote 10th and 90th percentiles and circle indicates mean. Stim., stimulation; wash., washout.

To assess whether repeated closed-loop stimulation could engage cerebellar learning mechanisms to produce sensorimotor adaptation, optical fibers were implanted in the cerebellar cortex at the interface between lobule simplex and lobules 4 and 5 (Extended Data Fig. 6c,d). Experiments were structured in a block format, where animals reached unperturbed in a baseline block; followed by a stimulation block, where closed-loop stimulation of pontocerebellar axons (50-ms train) was delivered on every reach when the hand passed a 1-cm threshold in the outward direction; and, finally, a washout block, where stimulation was removed to assess any aftereffects of learning. Each block was roughly 15–30 reaches long, determined by each individual animal's endurance in the task (Fig. 3a; baseline, 23.1 ± 6.24 reaches; stimulation, 22.4 ± 5.77 reaches; washout, 20.56 ± 6.65 reaches; mean ± s.d.; $N = 5$ animals, 104 sessions). Early in the stimulation block, we found that stimulation caused acute changes in reach kinematics: in four of five animals it caused hypermetric reaches in the outward position, and in one animal it caused hypometric reaches (Fig. 3b–c and Extended Data Fig. 7a examples 1 and 2). To assess the relative change in hand position over the stimulation block, we measured the magnitude of the stimulation effect over the block, defining the initial direction of the stimulation effect on hand position as positive and the opposing direction as negative. We found that the magnitude of the stimulation effect decreased over the stimulation block. When the stimulation was removed, reaches deviated in the direction opposite the initial stimulation direction early in the washout block, before eventually correcting back to baseline at the end of the washout block in both outward position and velocity (Fig. 3d–f; $N = 5$ animals, 104 sessions; outward position, $P = 1.7 \times 10^{-3}$, $F = 11.3$, RM one-way ANOVA; early stimulation to middle stimulation, $P = 8.9 \times 10^{-3}$, $d = 2.0$; early stimulation to early washout, $P = 0.030$, $d = 1.5$; early stimulation to middle washout, $P = 0.017$, $d = 1.7$; early stimulation to late washout, $P = 0.031$, $d = 1.4$; early washout to late washout, $P = 0.042$, $d = -1.3$; Tukey's multiple comparisons test; outward velocity, $P = 4.7 \times 10^{-3}$, $F = 12.1$, RM one-way ANOVA; early stimulation to middle stimulation, $P = 0.024$, $d = 1.6$; early stimulation to early washout, $P = 0.041$, $d = 1.3$; early stimulation to middle washout, $P = 3.5 \times 10^{-3}$, $d = 2.6$; early stimulation to late washout,

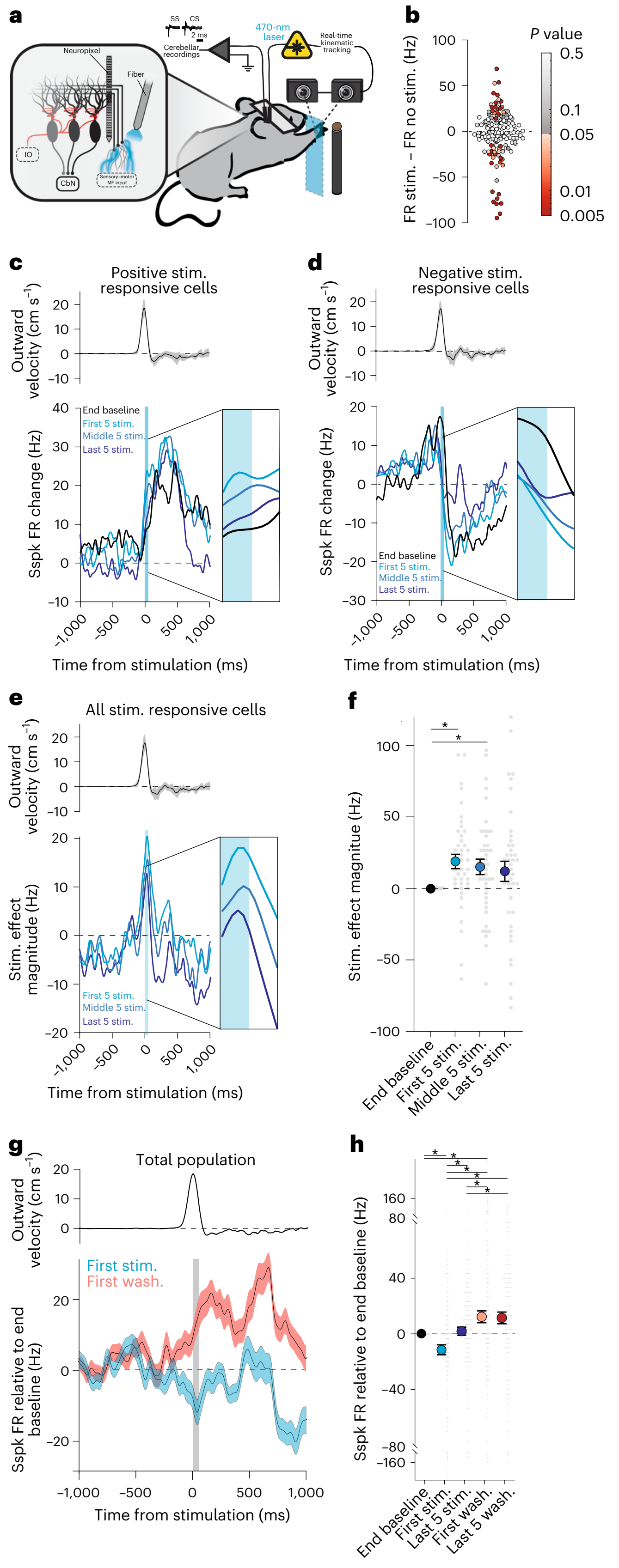

Fig. 4 | PCs show electrophysiological correlates of behavioral adaptation over the stimulation and washout blocks. **a**, Mossy fibers were stimulated at threshold crossing during outreach while recording PCs with Neuropixel probes. **b**, Mossy fiber stimulation effect during reach of all reach-modulated PCs. The difference in simple spike rate during the stimulation window is compared with the same epoch during baseline reaches. Significant differences are denoted by the color map on the right. $n = 159$ cells. **c**, Population summary of activity of PC firing rate adaptation over stimulation block for all PCs positively modulated by stimulation. Top, mean reach velocity for all sessions. Bottom, average change in simple spike rates for the last five baseline reaches (black) and the first five (cyan), middle five (light blue), and last five (dark blue) stimulated reaches. Blue shading denotes the time of mossy fiber stimulation. $n = 17$ cells. **d**, Same as in **c**, but for the population of PCs negatively modulated by stimulation. $n = 25$ cells. **e**, Same as in **c**, but measuring the magnitude of stimulation across stimulation increase and stimulation decrease cells. Here the effect of stimulation is measured in the direction of the initial stimulation effect, thus a positive deflection for stimulation increase cells means an increase in firing rate relative to baseline, and a positive deflection for stimulation decrease cells means a decrease in firing rate relative to baseline. **f**, Quantification of the data shown in **e**. $P = 7.2 \times 10^{-3}$, RM one-way ANOVA; for end baseline versus first five stimulations, $P = 2.6 \times 10^{-3}$; for end baseline versus middle five stimulations, $P = 0.037$; for end baseline versus last five stimulations, $P = 0.32$; Tukey's multiple comparisons test. **e**,**f**, $n = 42$ cells. **g**, Population activity across all reach-modulated cells. The first stimulated trial shows a negative deflection in net firing rate relative to baseline. Conversely, the first washout reach shows a net positive deflection. Gray box indicates the time of stimulation or analogous time in the washout block. **h**, Quantification of simple spike firing rates in the stimulation window for the data shown in **g** and the last five stimulated reaches and washout reaches. $P = 2.3 \times 10^{-9}$, RM one-way ANOVA; for end baseline versus first stimulation, 0.012; for end baseline versus first washout, $P = 0.039$; for first stim versus last five stimulations, $P = 7.4 \times 10^{-4}$; for first stimulation versus first washout, $P = 3.0 \times 10^{-6}$; for first stimulation versus last five washouts, $P = 1.9 \times 10^{-7}$; for last five stimulations versus first washout, $P = 0.019$; for last five stimulations versus last five washouts, $P = 0.015$; Tukey's multiple comparisons test. **g**,**h**, $n = 159$ cells. *$P < 0.05$. All error bars and bands represent mean ± s.e.m.

$P = 0.030$, $d = 1.5$; late stimulation to early washout, $P = 0.048$, $d = 1.3$, Tukey's multiple comparisons test). The magnitude of the initial stimulation effect on outward position predicted the magnitude of the initial washout aftereffect across animals (Fig. 3g, $R^2 = 0.820$, slope = −0.608 with 95% confidence interval [−1.13, −0.0853], $P = 0.034$, $F = 13.7$); however, hypometric effects were generally larger than hypermetric effects (both during stimulation and washout), possibly due to biomechanical constraints of the limb and reaching apparatus imposing a ceiling effect on hypermetric movements. Interestingly, the aftereffect did not appear until the time that stimulation would have been delivered during outreach (Fig. 3c and Extended Data Fig. 7d). In control experiments using red light (635 nm), we observed no kinematic deviations or adaptation profiles as seen with blue-light stimulation (Extended Data Fig. 7e). Further, blue-light stimulation at rest produced negligible movements (Extended Data Fig. 7f; $N = 4$ animals, 21 sessions; maximum outward velocity during stimulation of 0.26 cm s^{-1}).

To summarize, we have shown that animals adapt to a precisely timed internal perturbation of pontocerebellar mossy fibers, and this learning is reflected in opposing aftereffects when the perturbation is removed. Adaptation was temporally precise, with changes in limb kinematics early in the washout block timed to the predicted point of perturbation.

PC adaptation to mossy fiber stimulation

To investigate cellular correlates of learning in PCs during behavioral adaptation to this circuit-level perturbation, we performed stimulation experiments while recording near the optical fiber with a Neuropixel probe (Fig. 4a). To assure that any firing rate changes were not attributable to unstable cell isolation across the experiment, we assessed the stability of every PC using two metrics: a correlation of spike template waveforms, and the displacement of units along the electrode in the baseline and washout blocks (Extended Data Fig. 8; Methods). Of 314 putative PCs, 203 were stable across the experiment, 159 of which were modulated with reach. In the analyses that follow, we analyzed stimulus responsivity over the stimulus block in all stimulus-responsive PCs, and population-level changes over adaptation of all reach-modulated PCs. First, to assess optogenetic stimulus responsivity in these neurons, we compared simple spike firing rates between baseline and stimulated reaches within the 50-ms stimulation epoch. Consistent with mossy fiber stimulation at rest, we observed a diverging effect pattern with stimulation during reach: 17 cells showed significant increases in simple spike firing and 25 cells showed decreases (Fig. 4b, $P < 0.05$, paired t-test). In both groups, the efficacy of stimulation dropped over the course of the stimulation block, consistent with adaptation (Fig. 4c,d). To statistically analyze the progression of the stimulus effect over the stimulation block, we defined the direction of the initial response as positive for all cells (pooling cells that were inhibited and excited by stimulation) and then measured the response magnitude over time. The response magnitude dropped across the stimulation block such that, in later trials, firing rates were not significantly different from baseline (Fig. 4e,f; $N = 5$ animals, 42 stimulation-modulated cells; $P = 7.2 \times 10^{-3}$, $F = 5.5$, RM one-way ANOVA; for end baseline versus first five stimulated trials, $P = 2.6 \times 10^{-3}$, $d = -0.56$; for end baseline versus middle five stimulated trials, $P = 0.037$, $d = -0.41$; for end baseline versus last five stimulated trials, $P = 0.32$, $d = -0.26$; Tukey's multiple comparisons test). Notably, stimulation-affected cells did not show consistent aftereffects opposing the direction of the initial stimulation effect when the perturbation was removed.

Next, we analyzed how mossy fiber perturbations affected simple spike firing across the population of all reach-modulated PCs (stimulus-responsive and nonresponsive cells). We observed transient effects of stimulation and opposing aftereffects that were visible on the first trial of the stimulation and washout blocks, respectively (Fig. 4g). Across the population, the net effect of the first stimulation was a reduction of simple spike firing rate relative to baseline (Fig. 4g,h; $N = 6$ animals, 159 reach-modulated cells; for rates during the stimulation epoch, $P = 2.3 \times 10^{-9}$, $F = 13.8$, RM one-way ANOVA; for end baseline versus first stimulation, $P = 0.012$, $d = 0.26$; for end baseline versus first washout, $P = 0.039$, $d = -0.23$; for first stimulation versus last five stimulations, $P = 7.4 \times 10^{-4}$, $d = -0.47$; for first stimulation versus first washout, $P = 3.0 \times 10^{-6}$, $d = -0.42$; for first stimulation versus last five washouts, $P = 1.9 \times 10^{-7}$, $d = -0.47$; for last five stimulations versus first washout, $P = 0.019$, $d = -0.25$; for last five stimulations versus last five washouts, $P = 0.015$, $d = -0.25$; Tukey's multiple comparisons test). This effect was rapidly adapted such that, by the end of the stimulation block, mean simple spike firing returned to baseline levels. On the first washout reach, there was marked increase in simple spike rates, an aftereffect opposite the direction of the initial stimulation effect. This aftereffect was only marginally lower by the end of the washout block; however, simple spike firing outside of the stimulation window showed a more visible normalization to baseline levels (Extended Data Fig. 9a). This pattern of opposing rate deviations from baseline between the first stimulation and first washout reach were also seen in Cspk-identified PCs (Extended Data Fig. 9c,d). The dataset was underpowered to relate Cspk probability to these changes but, in the PCs in which Cspks were observed, the mean Cspk rate in the 250 ms after stimulation was not significantly different across the blocks (Extended Data Fig. 9b; $N = 5$ animals, $n = 13$ Cspk-sorted cells, $P = 0.31$, $F = 1.2$, RM one-way ANOVA). Overall, these data demonstrate acute neural effects of stimulation that adapt across the stimulation block, and population-level net aftereffects that oppose the initial firing rate deflection caused by stimulation, consistent with kinematic adaptation to perturbation and opposing aftereffects seen in reaches.

Random perturbations dissociate adaptation and aftereffect

In the experiments above, we showed that adaptation is temporally specific (for example, Extended Data Fig. 7b). We hypothesized that the temporal specificity of perturbation within the reach produced a fixed association between active inputs and error, facilitating adaptation. Therefore, we predicted that, by presenting spatially inconsistent stimuli trial to trial, mice would not adapt to stimulation. To test this, we repeated block-stimulation experiments but, rather than stimulating when the hand passed the 1-cm outward plane, we stimulated at a pseudorandomized position in the outward direction uniformly distributed between 0.3 and 1.8 cm (Fig. 5a,b). To assess the effect of stimulation at different points in the reach, we aligned reaches to the time of stimulation and measured the difference in position compared with aligned baseline block reaches. Baseline subtracted reach profiles showed a characteristic change in outward position aligned to the time of stimulation, similar to results in fixed-position stimulation experiments. Surprisingly, even though perturbation positions were distributed across the stimulation block, we found that animals still exhibited adaptation to the stimulation early in the stimulation block, although this adaptation plateaued to intermediate levels between middle and late block epochs in outward position and velocity (Fig. 5c,d; $N = 5$ animals, 60 sessions; for outward position, $P = 0.016$, $F = 10.8$, RM one-way ANOVA; for baseline to early stimulation, $P = 3.6 \times 10^{-4}$, $d = -3.9$, Tukey's multiple comparisons test; for outward velocity, $P = 0.016$, $F = 7.5$, RM one-way ANOVA; for baseline to early stimulation, $P = 0.040$, $d = -1.1$; for early stimulation to late stimulation, $P = 0.017$, $d = 1.4$, Tukey's multiple comparisons test). To assess the presence of aftereffects, we analyzed the positional and velocity differences between baseline and washout reaches near the mean of the distribution of stimulus thresholds (50–100 ms after crossing the 1-cm outward plane). Despite evidence for adaptation to the randomized stimulation, there were no consistent aftereffects; instead, reaches tended to have a greater distribution of positional differences that averaged to roughly zero (Fig. 5e and Extended Data Fig. 10; for outward position, $P = 0.65$, $F = 0.40$, RM one-way ANOVA; for outward velocity, $P = 0.76$, $F = 0.23$, RM one-way ANOVA).

Time-based generalization explains adaptation profiles

To better understand the nonintuitive adaptation profile of position-randomized stimulation, we modified a simple model of PC

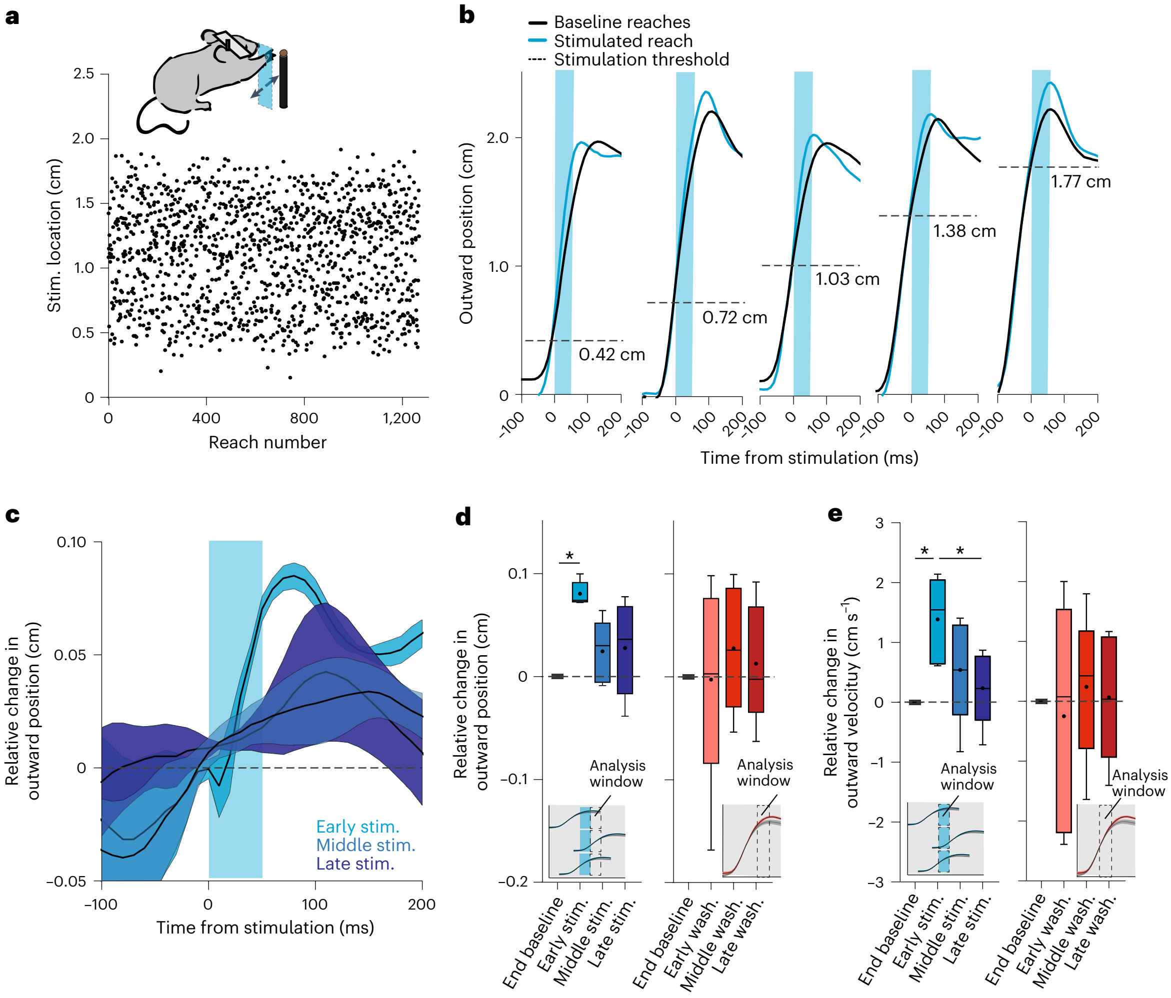

Fig. 5 | Dissociation of adaptation and aftereffects with randomized stimulation position. **a**, Stimulation location during outreach was distributed pseudorandomly between 0.3 and 1.8 cm in the outward direction during the stimulation block. **b**, Examples of reaches stimulated at five different locations during outreach. Each stimulated reach is compared with the last five baseline reaches of each session. The horizontal dashed line indicates the threshold crossing that triggered stimulation. Blue shading denotes the time of mossy fiber stimulation. **c**, Summary data of relative change in outward position for stimulation reaches in the early, middle and late block. **d**, Quantification of stimulation effect on outward position across adaptation block. For each reach, the analysis window was the 50–100 ms after stimulation onset aligned to the time of threshold crossing for each reach (inset). Quantification of aftereffects on outward position during washout block. Here the analysis window is the 50–100 ms after crossing the 1-cm threshold for each reach—the same as the analysis in fixed-position stimulation experiments. $P = 0.016$, RM one-way ANOVA; for baseline to early stimulation, $P = 3.6 \times 10^{-4}$, Tukey's multiple comparisons test. **e**, Same as **d**, but instead quantifying of outward velocity in the stimulus window, and aftereffects in the 50 ms after crossing the 1-cm threshold for each reach. $P = 0.016$, RM one-way ANOVA; for baseline to early stimulation, $P = 0.040$; for early stimulation to late stimulation, $P = 0.017$; Tukey's multiple comparisons test. $N = 5$ animals, 60 sessions. $^*P < 0.05$. All error bars and bands represent mean ± s.e.m. In box-and-whisker plots, box denotes median and 25th–75th percentiles, whiskers denote 10th and 90th percentiles and the circle indicates mean.

firing based on a previously published study[51]. As an input, the model takes parallel fibers and inhibitory interneurons, each active for 15 ms, that as a population tile a 400-ms hypothetical movement (Fig. 6a). The PC rate mimicked the net firing rate suppression that we see in population activity during reach. At equilibrium, the populations of parallel fibers and interneurons are perfectly balanced during the movement and cause no deviation in the PC firing rate from trial to trial. The model used a learning rule such that any elevation of the PC rate from this equilibrium would lead to depressing the weights of parallel fibers active at the time of deviation through a Cspk-like error signal, as in cerebellar long-term depression. Conversely, parallel fibers with depressed weights relax back to baseline levels in the absence of Cspks. We titrated the learning rate to match that observed in fixed-position stimulation experiments (Methods).

First, we modeled fixed-position optogenetic perturbation experiments by artificially increasing activity in a random subset of parallel fibers and interneurons 50 ms in the middle of the hypothetical movement (Fig. 6a). Differential parallel fiber to interneuron activation ratios lead to a net activation of the PC to engage the Cspk-on learning rule (Methods). Initially, this modification of PC inputs caused a large deviation in the PC firing rate in the stimulated window, resulting in an error and synaptic depression of the concomitantly active parallel fibers (Fig. 6b). Over several repeated perturbation trials, this reweighting minimized the effect of the perturbation, correcting PC firing rate back to baseline. After 20 trials, we removed the perturbation. The model output then exhibited opposing aftereffects in PC firing rate at the previous time of perturbation, before relaxing back to baseline eventually. The adaptation profile was similar quantitatively to the empirically observed behavior. Importantly, we note that the aftereffect seen in the PC firing profile is a consequence of depressed weights in both perturbed parallel fibers and other unperturbed parallel fibers that were coincidentally active at the time of the perturbation (Fig. 6c,d).

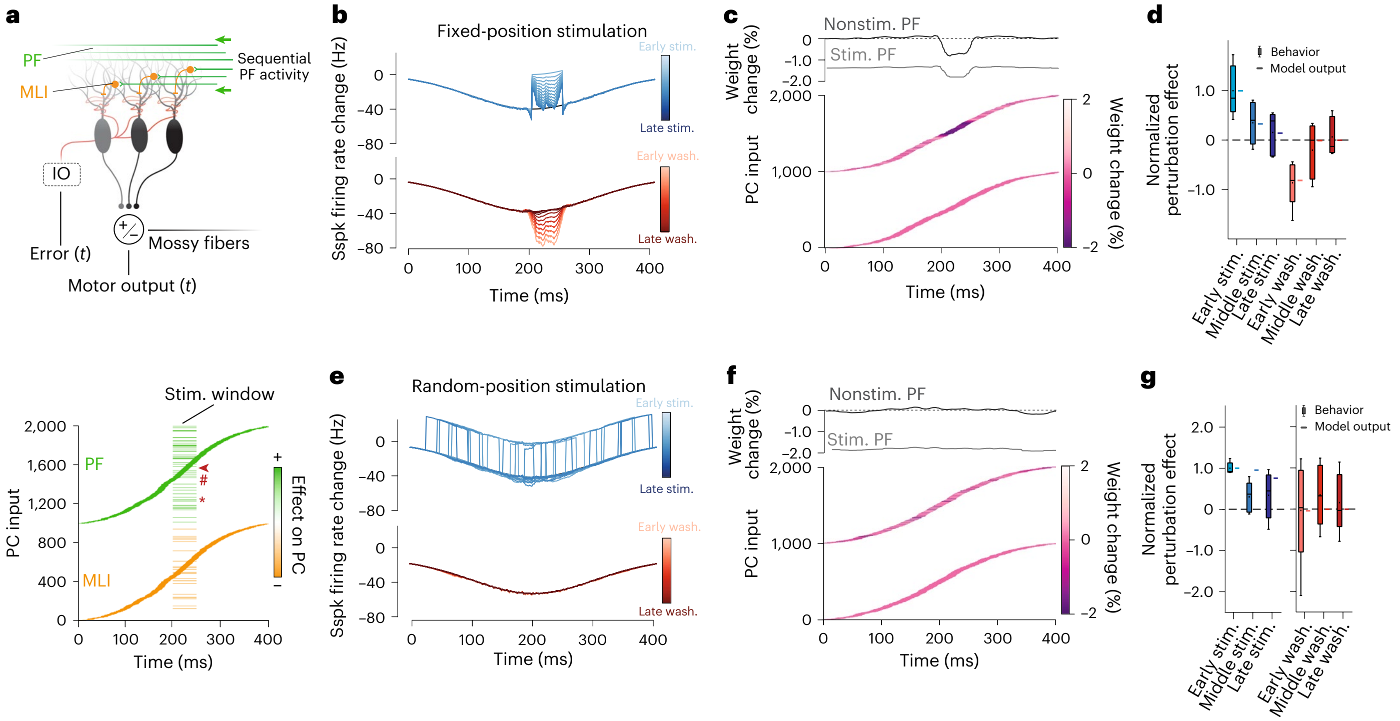

Fig. 6 | A cerebellar model accounts for adaptation and aftereffect dissociation. **a**, Schematic diagram of the temporal cerebellar learning model. The model input is a population of 2,000 cells, divided into two balanced populations of 1,000 parallel fibers and 1,000 interneurons, activated during a brief window during a simulated 400-ms movement. The output of the PC module that receives this information is compared with the input in the cerebellar nuclei. At equilibrium, the two populations are perfectly balanced (parallel fibers cause net activation of the PC, and the interneurons cause a net decrease; bottom) and the PC module outputs an activity curve (Gaussian that mimics the firing rate suppression observed in empirical data) that spans the movement. Positive deviations from this curve (errors) lead to mismatch in the nuclei and subsequent activation of the inferior olive, which reduces the weights of parallel fibers active shortly before the error. To simulate optogenetic perturbation experiments (barcode-like pattern at 200 ms), a step of activity was added to a subset of parallel fibers and interneurons for 50 ms in the center of the movement (fixed stim.) or randomized across the block (random stim.). Note that stimulation can either activate a cell twice (for example, parallel fiber 1,257 indicated by an asterisk) or overlap with endogenous activity (for example, 1,490, ind#), and nonstimulated neurons can be active endogenously during the stimulus window (for example, 1,561, arrowhead). *t*, time. **b**, PC simple spike activity during the stimulation block (top, blue) and washout block (bottom, red) showing progressively adapting response magnitudes during the adaptation block, and progressively decaying aftereffects during washout. **c**, Parallel fiber weight changes at the end of the fixed-position stimulation block. Top, change in weights of 'artificially' stimulated and nonstimulated parallel fibers plotted by time of endogenous activation. Bottom, heat map of parallel fiber weight changes on the top and unchanged interneurons on the bottom. Note population weight change concentrated at time of stimulation, seen in both artificially stimulated and unstimulated fibers during the stimulation epoch. **d**, Comparison of model output to empirical observations for fixed-position stimulus conditions (Fig. 3). Model closely matches behavioral adaptation. $N = 5$ animals, 104 sessions. **e**, Same as **b**, but here the stimulation window is randomized across the reach. **f**, Same as **c**, but for random-position stimulation experiments. Note the absence of clustered weight changes in unstimulated parallel fibers. **g**, Comparison of model output to empirical observations for random-position stimulus conditions (Fig. 5) showing that both model and empirical observations show adaptation but not directional aftereffects. $N = 5$ animals, 60 sessions. In box-and-whisker plots, box denotes median and 25th–75th percentiles, whiskers denote 10th and 90th percentiles and the circle indicates mean. PF, parallel fiber.

Thus, the model was unable to distinguish the difference between parallel fibers that caused or did not cause a deviation from the target PC activity within the perturbation epoch.

Next, we modeled the position-randomized mossy fiber stimulation paradigm (Fig. 6e–g). As with the empirical results, we saw a reduction in the magnitude of the perturbation effect, consistent with high probabilities of Cspks around the time of a perturbation; that is, the perturbed inputs are subject to learning because they are always aligned to the error that follows (Fig. 6e). Although the magnitude of adaptation was smaller than that observed in the fixed-position model, we found that the model learning plateaued late in the perturbation block, similar to empirical observations (Fig. 6g). When the perturbation was removed, there were minimal aftereffects, also consistent with experimental data. Model weights at the end of the perturbation show that this absence of aftereffects is explained by the lack of accumulated learning in coincidentally active parallel fibers; that is, when perturbations are distributed across the movement, coincidently active parallel fibers are different from trial to trial and, therefore, subjected to transient plasticity only (Fig. 6f). Thus, in randomized stimulation, the presence of adaptation illustrated a mechanism by which the cerebellum distinguishes cause and effect using time: adaptation is explained by the conserved causal relationship between stimulated PC inputs and error, whereas the absence of an aftereffect is the result of unaccumulated trial-over-trial learning in coincidentally active nonstimulated inputs. By contrast, aftereffects in the fixed-position paradigm are a consequence of the system generalizing attribution of error to fibers that were merely coincidently active relative to perturbation but did not necessarily drive error.

Discussion

We discovered a net PC population firing rate suppression during mouse reaching movements that scaled with the velocity of outreach and occurred shortly before the transition to the decelerative phase of movement. This suppression is reminiscent of emergent PC population kinematic coding in the oculomotor vermis during saccades[37]. We speculate that this suppression is a type of conditioned response:

sensorimotor information relayed through mossy fibers becomes a learned cue for PCs to scale the decelerative phase of movement via disinhibition of the anterior interposed nucleus. We further demonstrate kinematic effects of mossy fiber stimulation that decrease over trials, akin to sensorimotor adaptation, with concordant changes in PC activity that imply cerebellar associative learning. We observed a surprising dissociation of adaptation and aftereffects when randomizing the position of stimulation during reach, designed to test the reliance of adaptation on perturbation context. A model demonstrated that aftereffects are a consequence of misattribution of error to consistently coactive parallel fibers. Conversely, the dissociation of adaptation and aftereffects reflects a lack of accumulated plasticity at a single point during the movement.

By demonstrating remapping of inputs to outputs of the cerebellar cortex, we link concepts developed in delay eyeblink conditioning to adaptation of a skilled volitional movement. Specifically, the mossy fiber stimulation used here to drive reach perturbations is analogous to mossy fiber stimulation used as a conditioned stimulus in eyeblink conditioning. We speculate that motor plan or early kinematic information acts endogenously as a conditioned stimulus associated with reach outcome that, when erroneous, drives cerebellar learning[43]. We note some nuanced differences between paradigms, however. For instance, adaptation to pontocerebellar stimulation occurs within tens of trials, many fewer than conditioned eyeblink responses, which require hundreds of pairings[52]. However, nonhuman primates and cats exhibit rapid adaptation consistent with our results in other sensorimotor adaptation paradigms[24,53]. Multiple factors may explain this difference, including the richness of granule cell population coding during movements versus quiescent associations[54], and building on pre-existing associations of pontocerebellar inputs to reach kinematics versus de novo mapping cues to outcomes in classical conditioning.

Another conspicuous departure from learning seen in eyeblink conditioning is that mossy fiber stimulation during reach drives an error. Thus, the unconditioned stimulus is not externally imposed but is rather the erroneous behavior that results from the perturbed mossy fiber activity. In this sense, the mossy fiber activity that interferes with cerebellar control acts as both a conditioned stimulus and generates a movement error that acts as an unconditioned stimulus to drive learning.

Isolating a locus of skilled reach adaptation to the cerebellum poses an important conceptual hurdle. Cerebral cortex is a major input to the pontine nuclei—the focus of perturbation in this study—thus learning in the motor cortex must be accounted for in cerebellar contributions to movement. Likewise, cerebellar outputs relay information back to motor cortex indirectly via the thalamus[55]. Previous work demonstrated that reach-associated pontocerebellar stimulation drives activity in motor cortex[28], meaning each learner in this loop stays apprised of the activity in the other. Could plasticity sites outside the cerebellum account for our observations? Our data argue for a locus of learning in the cerebellum in two major ways. First, we observe reduced efficacy of mossy fiber drive onto PCs over many repeated trials. A parsimonious explanation is that highly plastic parallel fiber synaptic weights are changing during adaptation rather than cortical commands overriding these proximal perturbations. Second, if PC firing rate changes were caused by modulated afferents to the cerebellum, it would be difficult to reconcile such a mechanism with adaptation to randomized stimulation because these compensatory cerebellar inputs could not predict the time of stimulation. Of course, one caveat to these findings is the prevalence of putative PCs in our dataset. Although there is currently not a known cell type that is easily mistaken for a PC based on simple spike firing statistics, future discoveries could prompt reinterpretation of these data.

How might multiple connected brain regions, all of which are implicated in learning, accomplish learning a task in parallel? In our study, mice were expertly trained when we introduced optogenetic perturbation of inputs. Thus, stimulating pontocerebellar fibers, we corrupted the relationship of action directed by motor cortex and the established cerebellar response tuned to that action. Through adaptation, the cerebellum learned to assist movements with these newly modified inputs as evidenced by the diminishing kinematic effect on the limb; when stimulation was removed, the novel mismatch of cortical and adapted cerebellar contribution to the movement again manifests as movement errors.

Our data unite two threads of cerebellar theory, classical conditioning and motor adaptation under the umbrella of associative learning, where active inputs to the cerebellum can be reformatted flexibly to accomplish a goal more accurately.

Online content

Any methods, additional references, Nature Portfolio reporting summaries, source data, extended data, supplementary information, acknowledgements, peer review information; details of author contributions and competing interests; and statements of data and code availability are available at https://doi.org/10.1038/s41593-023-01347-y.

References

1. Holmes, G. The symptoms of acute cerebellar injuries due to gunshot injuries. *Brain* **40**, 461–535 (1917).
2. Becker, M. I. & Person, A. L. Cerebellar control of reach kinematics for endpoint precision. *Neuron* **103**, 335–348.e5 (2019).
3. Baizer, J. S., Kralj-Hans, I. & Glickstein, M. Cerebellar lesions and prism adaptation in macaque monkeys. *J. Neurophysiol.* **81**, 1960–1965 (1999).
4. Tseng, Y. W., Diedrichsen, J., Krakauer, J. W., Shadmehr, R. & Bastian, A. J. Sensory prediction errors drive cerebellum-dependent adaptation of reaching. *J. Neurophysiol.* **98**, 54–62 (2007).
5. Morton, S. M. & Bastian, A. J. Cerebellar contributions to locomotor adaptations during splitbelt treadmill walking. *J. Neurosci.* **26**, 9107–9116 (2006).
6. Smith, M. A. & Shadmehr, R. Intact ability to learn internal models of arm dynamics in Huntington's disease but not cerebellar degeneration. *J. Neurophysiol.* **93**, 2809–2821 (2005).
7. Miall, R. & Wolpert, D. Forward models for physiological motor control. *Neural Netw.* **9**, 1265–1279 (1996).
8. Kawato, M. & Gomi, H. The cerebellum and VOR/OKR learning models. *Trends Neurosci.* **15**, 445–453 (1992).
9. Ohyama, T., Nores, W. L., Murphy, M. & Mauk, M. D. What the cerebellum computes. *Trends Neurosci.* **26**, 222–227 (2003).
10. Shadmehr, R., Smith, M. A. & Krakauer, J. W. Error correction, sensory prediction, and adaptation in motor control. *Annu. Rev. Neurosci.* **33**, 89–108 (2010).
11. Lee, K. H. et al. Circuit mechanisms underlying motor memory formation in the cerebellum. *Neuron* **86**, 529–540 (2015).
12. Lavond, D. G., Knowlton, B. J., Steinmetz, J. E. & Thompson, R. F. Classical conditioning of the rabbit eyelid response with a mossy-fiber stimulation CS: II. lateral reticular nucleus stimulation. *Behav. Neurosci.* **101**, 676–682 (1987).
13. Mauk, M. D., Steinmetz, J. E. & Thompson, R. F. Classical conditioning using stimulation of the inferior olive as the unconditioned stimulus. *Proc. Natl Acad. Sci. USA* **83**, 5349–5353 (1986).
14. Coesmans, M., Weber, J. T., De Zeeuw, C. I. & Hansel, C. Bidirectional parallel fiber plasticity in the cerebellum under climbing fiber control. *Neuron* **44**, 691–700 (2004).
15. Ito, M. & Kano, M. Long-lasting depression of parallel fiber-Purkinje cell transmission induced by conjunctive stimulation of parallel fibers and climbing fibers in the cerebellar cortex. *Neurosci. Lett.* **33**, 253–258 (1982).
16. Blazquez, P. M., Hirata, Y., Heiney, S. A., Green, A. M. & Highstein, S. M. Cerebellar signatures of vestibulo-ocular reflex motor learning. *J. Neurosci.* **23**, 9742–9751 (2003).

17. Yang, Y. & Lisberger, S. G. Interaction of plasticity and circuit organization during the acquisition of cerebellum-dependent motor learning. *eLife* **2**, e01574 (2013).
18. Herzfeld, D. J., Kojima, Y., Soetedjo, R. & Shadmehr, R. Encoding of error and learning to correct that error by the Purkinje cells of the cerebellum. *Nat. Neurosci.* **21**, 736–743 (2018).
19. Raymond, J. L., Lisberger, S. G. & Mauk, M. D. The cerebellum: a neuronal learning machine? *Science* **272**, 1126–1131 (1996).
20. Gandolfo, F., Li, C. S. R., Benda, B. J., Padoa Schioppa, C. & Bizzi, E. Cortical correlates of learning in monkeys adapting to a new dynamical environment. *Proc. Natl Acad. Sci. USA* **97**, 2259–2263 (2000).
21. Li, C. S. R., Padoa-Schioppa, C. & Bizzi, E. Neuronal correlates of motor performance and motor learning in the primary motor cortex of monkeys adapting to an external force field. *Neuron* **30**, 593–607 (2001).
22. Mathis, M. W., Mathis, A. & Uchida, N. Somatosensory cortex plays an essential role in forelimb motor adaptation in mice. *Neuron* **93**, 1493–1503.e6 (2017).
23. Proville, R. D. et al. Cerebellum involvement in cortical sensorimotor circuits for the control of voluntary movements. *Nat. Neurosci.* **17**, 1233–1239 (2014).
24. Hewitt, A. L., Popa, L. S. & Ebner, T. J. Changes in Purkinje cell simple spike encoding of reach kinematics during adaption to a mechanical perturbation. *J. Neurosci.* **35**, 1106–1124 (2015).
25. Ito, M. Neural design of the cerebellar motor control system. *Brain Res.* **40**, 81–84 (1972).
26. Weiler, J., Gribble, P. L. & Pruszynski, J. A. Spinal stretch reflexes support efficient hand control. *Nat. Neurosci.* **22**, 529–533 (2019).
27. Low, A. Y. T. et al. Precision of discrete and rhythmic forelimb movements requires a distinct neuronal subpopulation in the interposed anterior nucleus. *Cell Rep.* **22**, 2322–2333 (2018).
28. Guo, J.-Z. et al. Disrupting cortico-cerebellar communication impairs dexterity. *eLife* **10**, e65906 (2021).
29. Becker, M. I., Calame, D. J., Wrobel, J. & Person, A. L. Online control of reach accuracy in mice. *J. Neurophysiol.* **124**, 1637–1655 (2020).
30. Tibshirani, R. Regression shrinkage and selection via the lasso. *J. R. Stat. Soc.* **58**, 267–288 (1996).
31. Popa, L. S., Streng, M. L. & Ebner, T. J. Long-term predictive and feedback encoding of motor signals in the simple spike discharge of Purkinje cells. *eNeuro* **4**, ENEURO.0036-17.2017 (2017).
32. Streng, M. L., Popa, L. S. & Ebner, T. J. Climbing fibers control Purkinje cell representations of behavior. *J. Neurosci.* **37**, 1997–2009 (2017).
33. Coltz, J. D., Johnson, M. T. & Ebner, T. J. Cerebellar Purkinje cell simple spike discharge encodes movement velocity in primates during visuomotor arm tracking. *J. Neurosci.* **19**, 1782–1803 (1999).
34. Hewitt, A. L., Popa, L. S., Pasalar, S., Hendrix, C. M. & Ebner, T. J. Representation of limb kinematics in Purkinje cell simple spike discharge is conserved across multiple tasks. *J. Neurophysiol.* **106**, 2232–2247 (2011).
35. Roitman, A. V., Pasalar, S., Johnson, M. T. V. & Ebner, T. J. Position, direction of movement, and speed tuning of cerebellar Purkinje cells during circular manual tracking in monkey. *J. Neurosci.* **25**, 9244–9257 (2005).
36. Musall, S., Kaufman, M. T., Juavinett, A. L., Gluf, S. & Churchland, A. K. Single-trial neural dynamics are dominated by richly varied movements. *Nat. Neurosci.* **22**, 1677–1686 (2019).
37. Herzfeld, D. J., Kojima, Y., Soetedjo, R. & Shadmehr, R. Encoding of action by the Purkinje cells of the cerebellum. *Nature* **526**, 439–441 (2015).
38. Brown, S. T. & Raman, I. M. Sensorimotor integration and amplification of reflexive whisking by well-timed spiking in the cerebellar corticonuclear circuit. *Neuron* **99**, 564–575.e2 (2018).
39. Person, A. L. & Raman, I. M. Purkinje neuron synchrony elicits time-locked spiking in the cerebellar nuclei. *Nature* **481**, 502–505 (2012).
40. Thier, P., Dicke, P. W., Haas, R. & Barash, S. Encoding of movement time by populations of cerebellar Purkinje cells. *Nature* **405**, 72–76 (2000).
41. Medina, J. F. & Lisberger, S. G. Links from complex spikes to local plasticity and motor learning in the cerebellum of awake-behaving monkeys. *Nat. Neurosci.* **11**, 1185–1192 (2008).
42. Kimpo, R. R., Rinaldi, J. M., Kim, C. K., Payne, H. L. & Raymond, J. L. Gating of neural error signals during motor learning. *eLife* **3**, e02076 (2014).
43. Avraham, G., Taylor, J. A., Breska, A., Ivry, R. B. & McDougle, S. D. Contextual effects in sensorimotor adaptation adhere to associative learning rules. *eLife* **11**, e75801 (2022).
44. Kitazawa, S., Kimura, T. & Yin, P. B. Cerebellar complex spikes encode both destinations and errors in arm movements. *Nature* **392**, 494–497 (1998).
45. Gaffield, M. A., Sauerbrei, B. A. & Christie, J. M. Cerebellum encodes and influences the initiation, performance, and termination of discontinuous movements in mice. *eLife* **11**, e71464 (2022).
46. Chabrol, F. P., Blot, A. & Mrsic-Flogel, T. D. Cerebellar contribution to preparatory activity in motor neocortex. *Neuron* **103**, 506–519.e4 (2019).
47. Miall, R. C., Keating, J. G., Malkmus, M. & Thach, W. T. Simple spike activity predicts occurrence of complex spikes in cerebellar Purkinje cells. *Nat. Neurosci.* **1**, 13–15 (1998).
48. Brodal, P. & Bjaalie, J. G. Organization of the pontine nuclei. *Neurosci. Res.* **13**, 83–118 (1992).
49. Sillitoe, R. V., Fu, Y. H. & Watson, C. in *The Mouse Nervous System* (eds Watson, C. et al.) Ch. 11 (Elsevier, 2012).
50. Rasmussen, A., Jirenhed, D. A., Wetmore, D. Z. & Hesslow, G. Changes in complex spike activity during classical conditioning. *Front. Neural Circuits* **8**, 90 (2014).
51. Herzfeld, D. J., Hall, N. J., Tringides, M. & Lisberger, S. G. Principles of operation of a cerebellar learning circuit. *eLife* **9**, e55217 (2020).
52. Mauk, M. D. & Buonomano, D. V. The neural basis of temporal processing. *Annu. Rev. Neurosci.* **27**, 307–340 (2004).
53. Shimansky, Y., Wang, J. J., Bauer, R. A., Bracha, V. & Bloedel, J. R. On-line compensation for perturbations of a reaching movement is cerebellar dependent: Support for the task dependency hypothesis. *Exp. Brain Res.* **155**, 156–172 (2004).
54. Albergaria, C., Silva, N. T., Darmohray, D. M. & Care, M. R. Locomotor activity modulates associative learning in mouse cerebellum. *Nat. Neurosci.* **21**, 725–735 (2018).
55. Nashef, A., Cohen, C., Isreal, Z., Harel, R. & Prut, Y. Cerebellar shaping of motor cortical firing is correlated with timing of motor actions. *Cell Rep.* **23**, 1275–1285 (2018).

Methods

Animals

All procedures followed National Institutes of Health Guidelines and were approved by the Institutional Animal Care and Use Committee at the University of Colorado Anschutz Medical Campus. Animals were housed in an environmentally controlled room, kept on a 12-h light–dark cycle and had ad libitum access to food and water, except during behavioral training and testing as described below. Adult C57BL/6 (Charles River Laboratories) mice of either sex (11 females, 8 males) were used in all experiments.

Surgical procedures

All surgical procedures were conducted under ketamine–xylazine anesthesia. After induction of anesthesia, the surgical site was cleaned and injected subcutaneously with bupivacaine (2.5 mg ml^{-1}). Pressure injections of approximately 150 nl of AAV2-hSyn-ChR2-mCherry were stereotaxically targeted to the left pontine nuclei (−4.0 mm anterior–posterior, −0.5 mm medial–lateral, −5.4 mm dorsal–ventral, measured from bregma) and animals were allowed to recover for a minimum of 8 weeks to ensure expression in mossy fiber terminals in the cerebellar cortex. Custom-made aluminum head plates were affixed to the skull, centered on the bregma, using luting (3 M) and dental acrylic (Teets Cold Cure). Optical fibers (105 µm core diameter; Thor Labs) attached to a ceramic ferrule (1.25 mm; Thor Labs) were implanted into the primary fissure, between lobules 4 and 5 and the lobule simplex (−6.25 mm anterior–posterior, 1.9 mm medial–lateral, measured from bregma), at a depth of 1.2 mm (ref. 11). For recording experiments, a craniotomy was made medial to the fiber placement and a recording chamber was secured with dental acrylic, as previously described[56].

Behavioral task

Animals were allowed a minimum of 2 days of recovery after head-fixation surgery, and were then food restricted to 80–90% of their baseline weight for reach training. Mice were habituated to the head-fixed apparatus by presenting food pellets (20 mg; catalog no. F0163, BioServ) that could be retrieved with their tongue, and pellets were then progressively moved further from the mouth until animals began reaching for food. Pellets were positioned to the right of the animal to encourage reaching with the right forelimb and moved to a consistent position specific to each mouse ~1.2–2.5 cm from the reach start. Sessions lasted until animals successfully retrieved 20 pellets or until 30 min had elapsed, whichever came first. Mice were trained for a minimum of 15 days and were considered fully trained once they could successfully retrieve 50% of pellets 3 days in a row.

Kinematic tracking and closed-loop optogenetic stimulation

Hand position was tracked in real time using an infrared-based machine-vision, motion-capture system (six Optitrack Slim3U Cameras mounted with LED ring arrays; Motive Software) at 120 frames per second as previously described[2]. Cameras were positioned in front and to the right of the animal and focused on the approximately 8 cm^3 spatial volume that covered the reach area of the right forelimb. Retroreflective markers (1 mm diameter) were used for camera calibration and affixed to the mouse hand for kinematic tracking. A custom-built calibration wand and ground plane were used to set position and orientation of the cameras in Optitrack Motive software. Camera calibration was refined monthly to account for any drift of the cameras over time. Calibrations that reported a mean triangulation error <0.05 mm were considered passes. The spatial origin was set to be at the center of the bar where mice placed their hand during rest. Spatial blocking and camera detection thresholds were adjusted to prevent erroneous tracking of minimally infrared-reflective objects.

Real-time hand positions were streamed into MATLAB (2018a) with a latency under 1 ms. Custom-written MATLAB code was used to detect when the hand passed a positional threshold 1-cm outward from the bar where the mice rested their hand and then send a 'go' signal to an Arduino microcontroller (Uno), which triggered a laser with transistor–transistor logic pulses. To ensure low-latency closed-loop stimulation we used an open-source C++ dynamic link library[57] edited to reflect the parameters of laser stimulation (50 ms stimulation, 100 Hz, 2 ms train). This system has a closed-loop latency of 9.5 ms from the time of threshold crossing (camera frame rate of 120 frames per second, 0.5 ± 0.1 ms (mean ± s.d.) MATLAB–Arduino communication). Hand positions and stimulation times were streamed into MATLAB and saved for postprocessing.

Kinematic analysis

All kinematic analysis was performed using custom-written MATLAB code. First, erroneously tracked objects were removed using a nearest neighbor analysis, which assessed the closest markers in subsequent frames and removed others, to produce a single positional trajectory of the hand marker over time. Any dropped frames where the marker was not detected were interpolated over, and then data were filtered using a second-order low-pass Butterworth filter (10 Hz)[58] using MATLAB's zero-phase filter function filtfilt. Last, interpolated points were removed, such that the filtered marker positional data reflected only data captured during the experimental session.

To segment continuous data into reaches, we found instances of the marker passing the 1-cm positional threshold in the outward direction and clipped 10-s segments centered on this time point. We defined outreach as the segment of this data from the time before threshold crossing that the hand exceeded 2 cm s^{-1} in outward and upward velocity to the time after threshold crossing where the hand stopped moving in the positive outward direction (outward velocity <0 cm s^{-1}). Occasionally, the marker would become obscured behind the pellet holder during reach or spurious detection of the nose would jump the marker position to the nose and be detected as a reach. Therefore, to prevent against analyzing reaches that had large segments of data missing, any threshold crossings where the marker dropped greater than 25% of points between the start and end of the outreach were not considered for further analysis.

Reach velocity and acceleration were calculated using the numerical gradient between position time points in each dimension. To produce aligned reach position curves, we interpolated data at 10 ms, centered on the time the hand passed the 1-cm positional threshold, crossing in an outward direction. The effect of stimulation was assessed by measuring changes in stimulation and washout reaches (early, middle and late) relative to the last five baseline reaches in the 50-ms interval after the end of stimulation. To assess the unadapted effect of stimulation or washout, early reaches were defined as the first reach in each block; middle and late reaches were the middle five and last five reaches of reach block, respectively. To align random-stimulation position reaches, we found the positional threshold of stimulation on each reach; aligned stimulation reaches and baseline reaches to the time they crossed this boundary during outreach, averaged across reaches; and then measured the difference in these curves, yielding the stimulation-aligned positional difference between end baseline and stimulation reaches. For washout reaches in random-position stimulation experiments, reaches were aligned to the time of the threshold crossing at 1 cm, such that the aftereffect could be compared to fixed-position stimulation experiments. To account for varying effects of stimulation seen across animals (hypermetric and hypometric movements), the direction of positional change in early stimulation reaches relative to baseline for each animal in random- or fixed-position stimulation experiments was defined as the positive direction, and the opposing direction as negative for that animal in each paradigm, allowing us to group data across animals with diverging effects. To assess the time course of stimulation effects within individual animals, we measured differences in position at each time point between the early stimulation reaches and baseline reaches using a Wilcoxon signed-rank test.

Electrophysiology recording procedure

Craniotomies were made over the cerebellum, ipsilateral to the reaching arm, in fully trained animals. A custom-made recording chamber was implanted over the craniotomy, the brain was covered with triple-antibiotic cream (Globe) and the recording chamber was sealed with Kwik-Sil silicone (World Precision Instruments) such that it could be preserved for multiple recordings.

Single-electrode recordings

Single-electrode recordings were performed with 3–5-MΩ platinum–tungsten optrodes (Thomas Recording). Once animals were head fixed, the electrode was targeted to −6.25 mm anterior–posterior, 1.9 mm medial–lateral (measured from bregma), and then lowered into the brain up to a depth of 1.8 mm using a motorized micromanipulator (Newport Motion Controller Model 861). Signals were band-pass filtered at 300–5000 Hz, amplified with a MultiClamp 700 A amplifier (Axon Instruments) and digitized (CED Power3 1401) and recorded using Spike2 software (CED). Once a putative PC was isolated, the brain tissue was allowed to relax for 15 min. Cell sorting was performed offline using Psort.

Neuropixel recordings

Neuropixels were lowered into the brain using a motorized micromanipulator (Sensapex uMp micromanipulator). Once the electrode shank spanned the putative PC layer, the tissue was allowed to relax for 15 min. Electrophysiology data were acquired using an OpenEphys system (https://open-ephys.org/gui). Data were sorted offline in Kilosort2 (ref. 59) and manually curated in phy (https://github.com/cortex-lab/phy).

Neural data analysis

After sorting, isolated units were analyzed offline using custom-written MATLAB code. In well-isolated, single-electrode units, simple spikes and identifiable Cspks were sorted using Psort. To identify Cspks in Neuropixel recordings, we crosscorrelated cells with high firing rates in the cortex with adjacent low-firing-rate clusters and looked for the presence of a Cspk-aligned simple spike pause and characteristic simple spike and Cspk waveforms. In many cells, Cspks could not be identified across the length of the experiment. In these cases, we identified PCs based on cortical location and electrophysiological criteria using the firing rate, CV2 and MAD[60]. Cerebellar cortical cells with a firing rate >40 spikes per second, CV2 of >0.20 and MAD of <0.008 were labeled as PCs (Extended Data Fig. 2). Using these metrics, we were able to positively identify 94.9% of Cspk-identified cells. We visualized these metrics in a two-dimensional space using the tSNE function in MATLAB (with the parameters distance = 'euclidean', exaggeration = 4, perplexity = 30, learning rate = 5,000). Instantaneous firing rates for PCs were calculated from the inverse of the interspike intervals, convolving with a 20-ms Gaussian and then sampling at 10-ms intervals. We found that most PCs with Cspks could be positively identified as such by using firing rate criteria alone, with a false negative rate of roughly 5.1% (5 of 98). Although we do not have a true false positive criterion to identify cells mistaken as PCs, as a proxy we note that the two distinct clusters of cells in the tSNE analysis corresponded roughly to PCs and non-PCs. By analyzing the cells that were identified as PCs in the non-PC cluster, we were able to estimate the false positive rate at roughly 3.8% (20 of 527).

In Neuropixel recording adaptation experiments, we analyzed reach-modulated PCs, defined as exhibiting a firing rate change during the reach epoch ≥1 s.d. of the mean firing rate of the cell. Cell recordings from the baseline (unstimulated) block from cerebellar stimulation experiments during reach were included in the datasets in Figs. 1 and 2. For analysis of the pooled population firing rate data in Fig. 1, we normalized reaches by velocity for each session and binned them into velocity quintiles. Thus, each cell was equally represented across all velocity quintiles. To find the magnitude of the firing rate decrease in grouped population PC data, we found the minimum value of the population firing rate traces for each percentile bin within the perireach window (−500 to +500 ms from threshold crossing). We found the time of firing rate suppression by measuring the point at which each trace decreased firing by 50% from peak to nadir in this perireach window. We characterized early Cspks as those that occurred within 500 ms before reach onset, corresponding to roughly the time of Cspk elevation seen across cells (Fig. 2a). Late Cspks were characterized as those that occurred during outreach or the 500-ms window after the end of outreach.

In pontocerebellar stimulation experiments, to assure that observed simple spike adaptation was not the result of changing unit isolation across the experiment, we assessed unit stability with two metrics: waveform correlation and unit displacement across the experiment. To assess waveform correlation, we isolated the template waveforms for each unit on the electrode with the greatest spike amplitude and the 32 surrounding electrodes (33 total). We averaged 1,000 randomly selected spike waveforms for each channel from the baseline block and the washout block, concatenated waveform templates across the 33 channels and then correlated the concatenated waveforms from the baseline and washout blocks (Pearson correlation). As a shuffled control, we correlated concatenated templates from neighboring units in the baseline and washout block. Neighboring units were defined as those whose 32 surrounding electrodes overlapped with the unit of interest. PCs whose across experiment waveform correlation did not exceed the 99th percentile (0.76) of the across-unit shuffled control correlation were excluded from further analysis.

To assess cell displacement across the experiment we calculated the position of unit (x, y) using

$$(x, y) = \left(\frac{\sum_{i=1}^{N} x_i a_i^2}{\sum_{i=1}^{N} a_i^2}, \frac{\sum_{i=1}^{N} y_i a_i^2}{\sum_{i=1}^{N} a_i^2} \right)$$

where N is the number of electrodes, x_i and y_i are the lateral and upward position of the electrode and a_i is the peak-to-peak spike waveform amplitude on the ith electrode. Unit displacement was defined as the Euclidean distance between unit positions in the baseline and washout blocks. As a shuffled control, the displacement between neighboring units (as defined above) across the experiment was calculated. PCs whose displacement was above the first percentile (2.36 µm) of shuffled control were excluded from further analysis.

LASSO regression

To quantify the variance of PC simple spike firing rate that could be explained by reach kinematics, we used LASSO regression[30]. LASSO has the advantage of performing both regressor selection and regularization, producing a sparse model of many correlated kinematic regressors. A total of 23 kinematic variables were used as regressors, including position, velocity and acceleration in the upward, outward and lateral directions; speed; and unsigned acceleration, with each velocity and acceleration term additionally broken into positive and negative components. A full list of regressors is included in Extended Data Fig. 3. Data for each reach were clipped into 2-s segments, centered at the time of a 1-cm threshold crossing in the outward direction. Regression was performed using a custom-written MATLAB code using the lasso function. All kinematic data were standardized to have a mean of zero and a variance of one, and regression was performed with a tenfold crossvalidation to avoid overfitting. To find the appropriate offset of firing rate and kinematics, instantaneous simple spike firing rates for each reach were offset by lags from 0 to −300 ms (firing rate leading kinematics) in 10-ms steps. The lag that minimized the mean squared error of the regression was selected for each cell. To calculate the variance of firing rate explained, the predicted firing rates from the best fit regression were calculated from the kinematic data and compared to empirical data. R^2 was calculated using

$$R^2 = 1 - \frac{\mathrm{SS_{res}}}{\mathrm{SS_{tot}}},$$

where $\mathrm{SS_{res}}$ is the sum of squared residuals and $\mathrm{SS_{tot}}$ is the total sum of squares.

For the spike-shuffled control, spike times on individual trials were shuffled in time so that each reach epoch had the same mean firing rate and then converted to instantaneous firing rates as described above. For the reach-shuffled control, reaches were assigned to firing rates recorded on different reaches. For both controls, regressions were performed at the lag that minimized the mean squared error for empirical data and repeated 100 times; R^2 values of each shuffled control were taken as the average of these 100 regressions. To assess the unique contribution of individual kinematic regressors to the fraction of variance explained in the empirical data regression, each regressor was time shuffled independently and regressions were repeated. The change in R^2 value between the regressor-shuffled regression compared to the complete empirical data model is the fraction of unique contribution to total variance explained for each kinematic variable[36].

Cerebellar model

The cerebellar model in the paper was derived from a previously published model[51] and written using custom code in Python. A major difference between our paper's model and the cited one is the assumption of a continuous temporal input of parallel fiber activity distributed across a hypothetical 400-ms movement, rather than a single parallel fiber input trial over trial. The model PC was fed 1,000 parallel fibers that positively modulated the PC firing rate and 1,000 molecular layer interneurons (MLIs) that negatively modulated the PC firing rate, which were each active for 15 ms during a 400-ms interval, mimicking hypothesized temporal basis sets produced by the granule cell layer[61–63]. In the absence of perturbation, these populations were perfectly balanced, leading to no changes of PC firing from trial to trial. PC firing at time t on the nth trial was calculated as the sum of the weighted contribution of all parallel fibers (PF) and MLIs at time t:

$$\mathrm{PC}_n(t) = \mathrm{PC}_0(t) + \sum_{i}^{1,000} w_n^i \mathrm{PF}_n^i(t) - \sum_{i}^{1,000} \mathrm{MLI}_n^i(t).$$

Here, w_n^i is the weight of parallel fiber i on the nth trial and PC_0 is the baseline firing rate of the PC.

Parallel fiber weights were subject to a learning rule based on deviations of the PC firing rate from trial to trial. Weights were adjusted after each trial according to two parameters: the probability of a Cspk (CS) as a function of trial error $\beta P(\mathrm{CS}|E_n)$ where β (0.15) dictates the strength of synaptic depression in response to a Cspk, and a decay term α_{PF} (0.95) that relaxes parallel fiber weights back to their initial value w_0^i:

$$w_{n+1}^i = w_n^i - (1-\alpha_{\mathrm{PF}})\left(w_n^i - w_0^i\right) - \beta P(\mathrm{CS}(t)|E_n(t)) \text{ if } \mathrm{PF}^i(t) > 0.$$

The probability of a Cspk is a function of t, where positive deviations in the PC rate from baseline at time t lead to elevation of Cspk rates from baseline, leading to long-term depression, and negative deviations of PC rate lead to reduction of Cspk rates from baseline levels, leading to long-term potentiation. Specifically, the error at time t ($E_n(t)$) was used to calculate the probability of a Cspk at each time in the movement interval:

$$P(\mathrm{CS}(t)|E_n(t)) = \frac{a}{1+e^{-\tau E_n(t)}} - \frac{a}{2}.$$

To obtain values for the parameters a and τ, we fit a curve to the change in position of early, middle and late stimulated reaches in fixed-position stimulation experiments and then took the derivative of this curve to obtain the error correction (trial-over-trial positional change) for a given error magnitude.

We ran the simulations mimicking the experimental block structure used for empirical data, including a baseline block with no perturbation, an experimental block with a perturbation on every trial and a washout block with the perturbation removed. For net positive perturbation trials, we added activity to a random subset of 150 parallel fibers and 50 MLIs at $t = 200$ ms for 50 ms that, when combined, drove an increase of 60 simple spikes per second in PCs at their initial weights (Extended Data Fig. 10). For net negative perturbation trials, we added activity to a random subset of 50 parallel fibers and 150 MLIs at $t = 200$ ms for 50 ms, which drove a net decrease of 60 simple spikes per second in PCs (Extended Data Fig. 9). For each simulation, after 20 perturbation trials, the perturbation was removed, and the model was run for an additional 20 washout trials. To simulate random-position perturbation experiments, the time of perturbation was changed on every trial.

Statistics and reproducibility

Data reported in the manuscript reflect statistical summaries from each animal across multiple sessions. For electrophysiological data, each neuron was treated as an independent sample. All data were tested for normality with the Kolmogorov–Smirnov test to choose the appropriate statistical analysis. All t-tests mentioned in the manuscript were two sided, unless stated otherwise. In box-and-whisker plots, the box displays the median and 25th and 75th percentiles and the whiskers extend to the 10th and 90th percentiles of the data, with the mean displayed as a dot in the box, unless otherwise stated.

Effect sizes for parametric tests were estimated using Cohen's d. For datasets with fewer than 50 samples, the Cohen's d value was corrected for small sample size by multiplying by

$$\left(\frac{N-3}{N-2.25}\right)\left(\sqrt{\frac{N-2}{N}}\right),$$

where N is the number of samples. Effect sizes for nonparametric tests were estimated by calculating r defined as

$$\left(\frac{Z}{\sqrt{N}}\right),$$

where Z is the Z statistic and N is the number of samples.

No statistical data were used to predetermine sample sizes, but the datasets are on par with similar studies. Randomization and controls are described in the main text. Experimenters were not blind to allocation during experiments and outcomes assessment. Nonparametric tests were used when datasets violated normality assumptions.

Reporting summary

Further information on research design is available in the Nature Portfolio Reporting Summary linked to this article.

Data availability

Source data used to make each of the figures are provided with this paper. Raw data are available upon reasonable request to the authors.

Code availability

The code for cerebellar model and custom analysis code can be found at https://github.com/dycala.

References

56. White, J. J. et al. An optimized surgical approach for obtaining stable extracellular single-unit recordings from the cerebellum of head-fixed behaving mice. *J. Neurosci. Methods* **262**, 21–31 (2016).
57. TestArduino (2015); https://github.com/cortex-lab/phy
58. Yu, B., Gabriel, D., Noble, L. & An, K. N. Estimate of the optimum cut-off frequency for the Butterworth low-pass digital filter. *J. Appl. Biomech.* **15**, 318–329 (1999).

59. Pachitariu, M., Steinmetz, N., Kadir, S., Carandini, M. & Harris, K. D. Kilosort: realtime spike-sorting for extracellular electrophysiology with hundreds of channels. Preprint at *bioRxiv* https://doi.org/10.1101/061481
60. Hensbroek, R. A. et al. Identifying Purkinje cells using only their spontaneous simple spike activity. *J. Neurosci. Methods* **232**, 173–180 (2014).
61. Kennedy, A. et al. A temporal basis for predicting the sensory consequences of motor commands in an electric fish. *Nat. Neurosci.* **17**, 416–422 (2014).
62. Lanore, F., Cayco-Gajic, N. A., Gurnani, H., Coyle, D. & Silver, R. A. Cerebellar granule cell axons support high-dimensional representations. *Nat. Neurosci.* **24**, 1142–1150 (2021).
63. Wagner, M. J. et al. Shared cortex-cerebellum dynamics in the execution and learning of a motor task. *Cell* **177**, 669–682 (2019).

Acknowledgements

We thank the members of A.L.P.'s laboratory for critical feedback on the manuscript; the Neurotechnology Center at the University of Colorado Anschutz Medical campus for use of core facilities, including the Advanced Light Microscopy Core and the Optogenetics and Neural Engineering Core. We thank M. Spindle and E. Judd for technical assistance. Work was supported by F31 NS113395-01 to D.J.C.; and NS114430, National Science Foundation CAREER grant 1749568, and by a grant from the Simons Foundation as part of the Simons-Emory International Consortium on Motor Control to A.L.P.

Author contributions

D.J.C. and A.L.P. designed experiments, interpreted data and wrote the manuscript. D.J.C. performed experiments, built the computational model, made figures and analyzed data. M.I.B. developed the closed-loop system, edited the manuscript and contributed to early conceptualization of the project.

Competing interests

The authors declare no competing interests.

Additional information

Extended data is available for this paper at https://doi.org/10.1038/s41593-023-01347-y.

Supplementary information The online version contains supplementary material available at https://doi.org/10.1038/s41593-023-01347-y.

Correspondence and requests for materials should be addressed to Abigail L. Person.

Peer review information *Nature Neuroscience* thanks Kamran Khodakhah and the other, anonymous, reviewer(s) for their contribution to the peer review of this work.

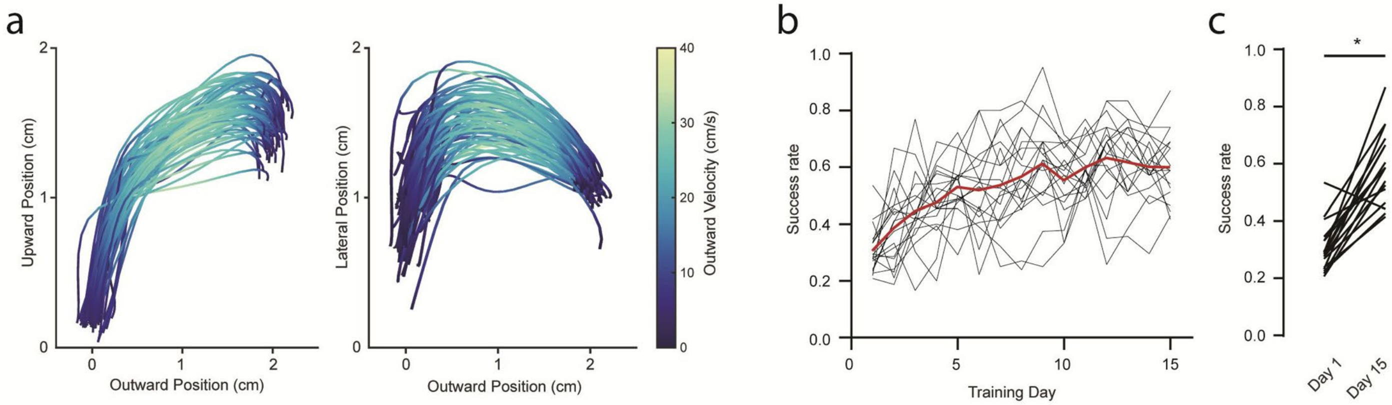

Extended Data Fig. 1 | Reach tracking and reach performance over sessions. **a**. The right hand was tracked with high-speed cameras as mice reached upwards and outwards towards a food pellet. Positional outreach trajectories from a single session viewed are shown from a lateral (left) or bottom-up (right) vantage point with traces colored by the magnitude of outward velocity. **b**. Mice were trained for a minimum of 15 days on the reaching task. Pellet retrieval success was tracked throughout training for each mouse, mean is shown in red. **c**. Quantification of success rate on day 1 of training and day 15. (**p-values:** (**c**) 6.4×10^{-8}, paired t-test; **Sample size:** n = 19 animals; * indicates p-value < 0.05).

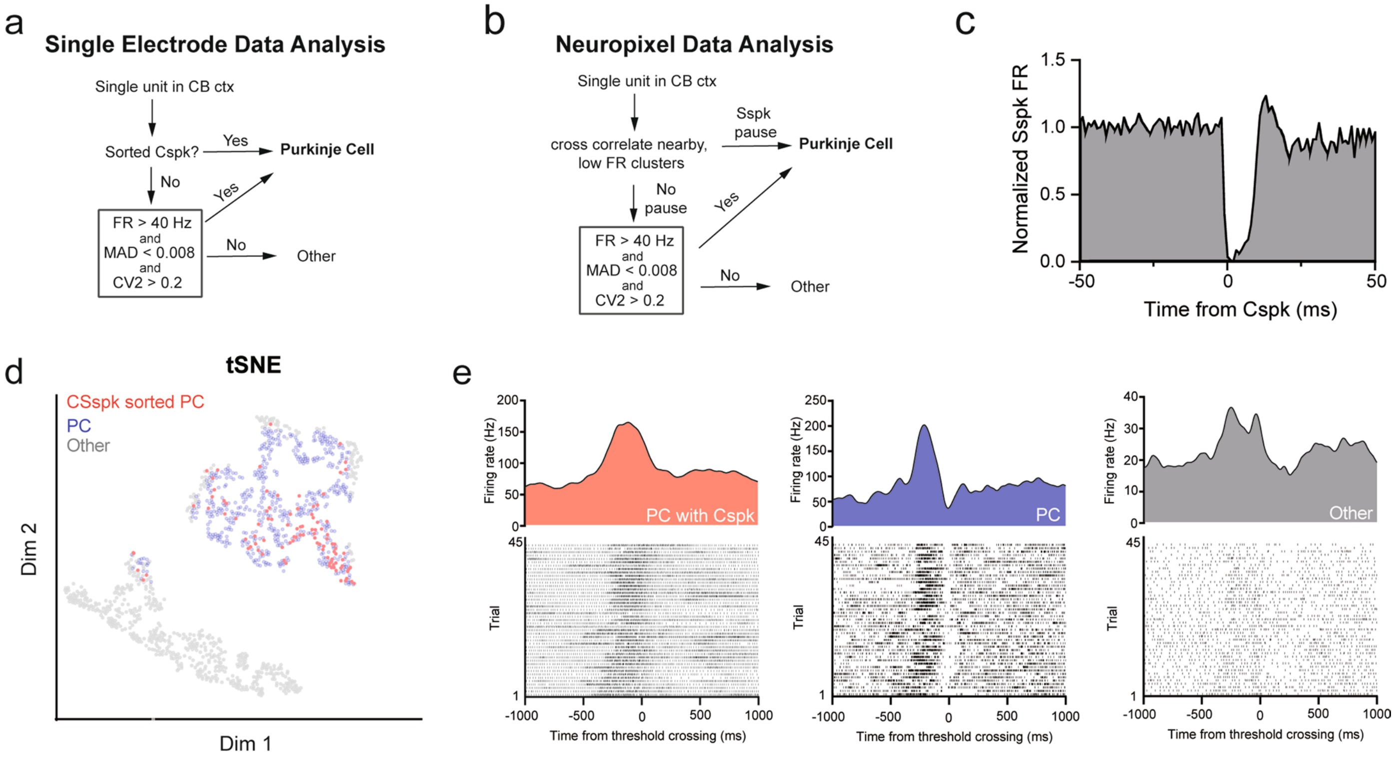

Extended Data Fig. 2 | PC identification by firing rate characteristics. **a**. Cerebellar recordings using single electrodes were first anatomically targeted to cerebellar cortex. If a recorded cell had visible Cspks they were classified as PCs. Otherwise, if cells had a firing rate > 40 Hz, a median absolute difference firing rate from the median interspike interval (MAD) < 0.008, and a CV2 > 0.2, they were classified as PCs[81]. **b**. Neuropixel-recorded single units were crosscorrelated with nearby (<200 microns) low firing rate (<5 Hz) single units. If this crosscorrelation exhibited the characteristic firing rate pause seen in PC simple spikes after a Cspk, these units were classified as the simple spikes and Cspks of a single PC. If no pause was seen, cells that exhibited the same firing rate, MAD, and CV2 profile described in a were classified as PCs. **c**. Example simple spike pause aligned to the time of a Cspk from a Neuropixel recording. **d**. Embedding MAD, CV2, and FR into a two-dimensional space using tSNE shows two distinct clusters, one corresponding largely to cells that were identified using the criteria in a and b and the other corresponding to other cells (n = 1268 sorted cells). **e**. Three example cells from a single session showing a neuron that was classified as a PC due to the presence of complex spikes (red, left), a neuron that was classified as a PC using firing rate criteria (blue, middle), and a neuron that was classified as other (grey, right). The simple spike raster and averaged simple spike firing rate PETH are shown on the bottom and top, respectively.

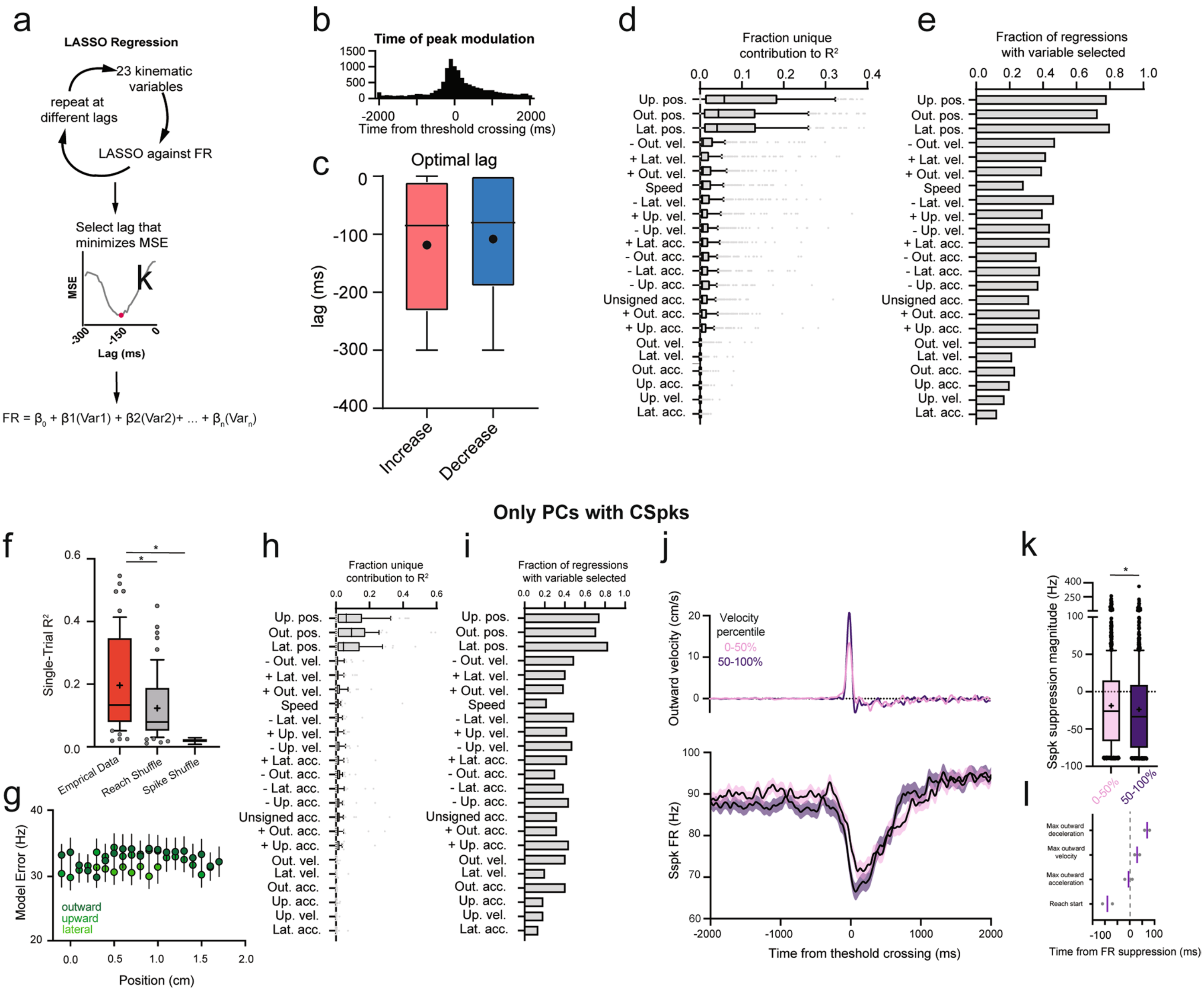

Extended Data Fig. 3 | Single cell and population reach encoding supplemental information. **a.** Schematic of LASSO regressions. 23 kinematic variables were regressed against firing rate at different lags from 0 to -300 ms. The lag that minimized the mean squared error (MSE) of the regressions was selected. **b.** Peak modulation time of all cells across all reaches. **c.** Optimal lags of the LASSO regression for each cell. **d.** Fraction of the unique contribution to total variance explained for each regressor. **e.** Fraction of regressions with each variable selected (mean shown for each regressor). **f.** Same as in Fig. 1d but only analyzing the subset of PCs that had Cspks identified. **g.** PCs with Cspks show no changes in model error across the reach, consistent with the total PC dataset. **h.** PCs with Cspks display kinematic variables with similar relative contributions to model variance explained compared to the total PC dataset. **i.** Variables included in the LASSO model in PCs with Cspks are consistent with data in the total PC dataset (mean shown for each regressor). **j.** Same as in Fig. 1h but only analyzing PCs with Cspks. The top and bottom 50% of outward reach velocities are analyzed. **k.** Quantification of the simple spike suppression of the data in f. **l.** Time of FR suppression for the data in f. (**p-values:** (**f**) empirical vs. reach shuffle: 4.4 ×10^{-11}, empirical vs spike shuffle: 2.4 ×10^{-11}, Wilcoxon signed rank test (**k**) 3.7 ×10^{-2}, Wilcoxon signed rank test; **Sample size:** (**b-e**) N = 11 animals, 465 cells (**f-k**) N = 8 animals, 59 cells; * indicates p-value < 0.05; all error bars and bands represent mean ± SEM; in box and whiskers plots box denotes median and 25th/75th percentiles, whiskers denote 10th and 90th percentiles, circle indicates mean).

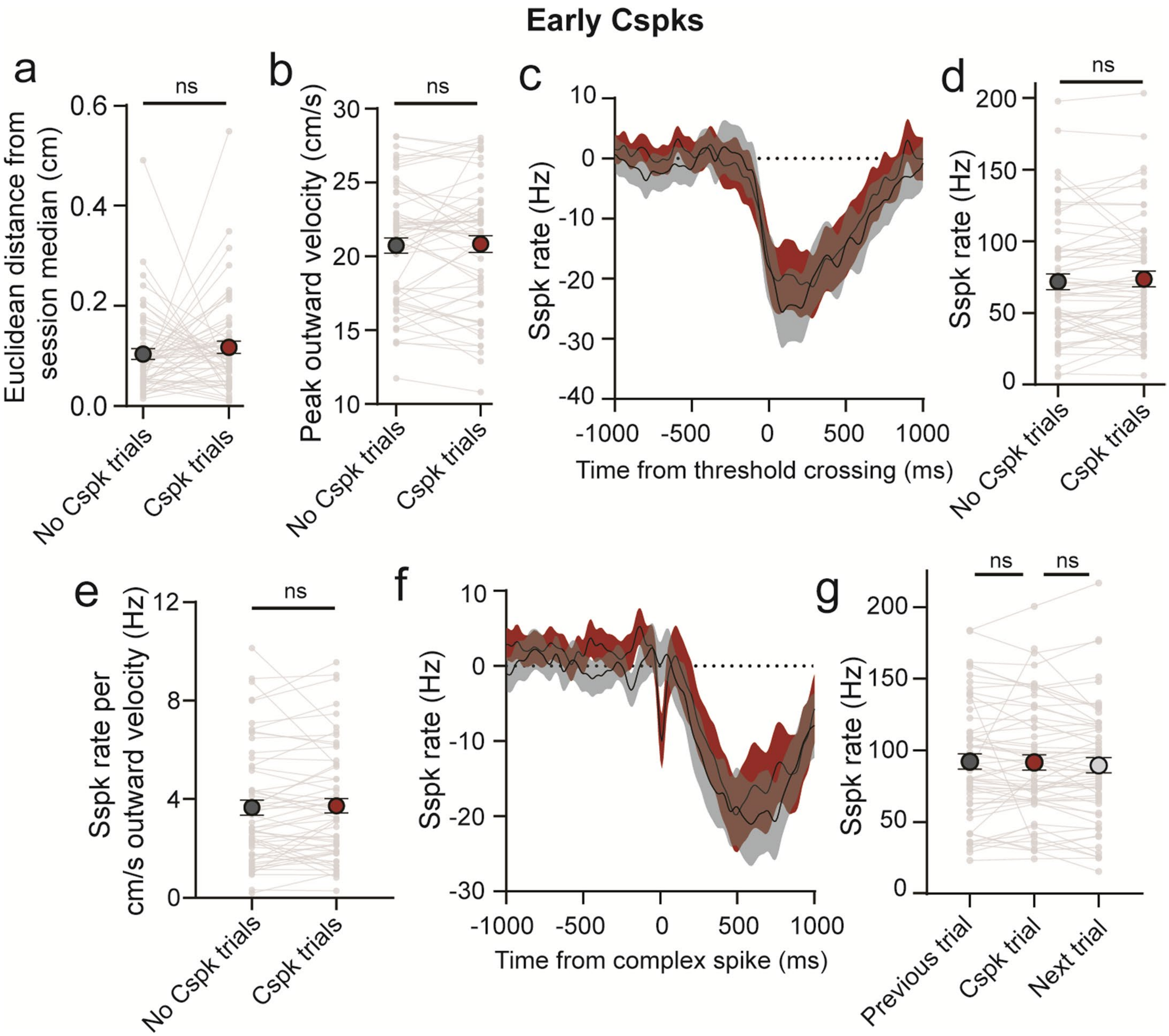

Extended Data Fig. 4 | Kinematic and simple spike correlates of early Cspks. **a**. Cspks in the 500 ms before reach onset were not associated with differences in target error as assessed with euclidean distance form session median compared to non-Cspk trials. **b**. No difference in peak outward velocity was observed between Cspks and non-Cspk trials. **c**. Simple spike firing rate in trials with early Cspk and non-Cspk trials. **d**. No difference in simple spike rate during outreach was seen in early Cspk trials compared with non-Cspk trials. **e**. No difference in simple spike rate per outward velocity was seen in early Cspk trials compared with non-Cspk trials. **f**. Simple spike firing aligned to the time of early Cspks compared to similarly aligned trials without early Cspk trials.**g**. No difference in simple spike rate in the 100 ms preceding early Cspks was seen compared to the similarly aligned previous or next trial. (**p-values:** (**a**) 0.32, Wilcoxon signed rank test (**b**) 0.75, paired t-test (**d**) 0.37, paired t-test (**e**) 0.29, Wilcoxon signed rank test (**g**) 0.47, RM one-way ANOVA, previous trial vs cspk trial: 0.97, cspk trial vs next trial: 0.42, Tukey's multiple comparisons test; **Sample size:** N = 8 animals, 58 cells; all error bars and bands represent mean ± SEM).

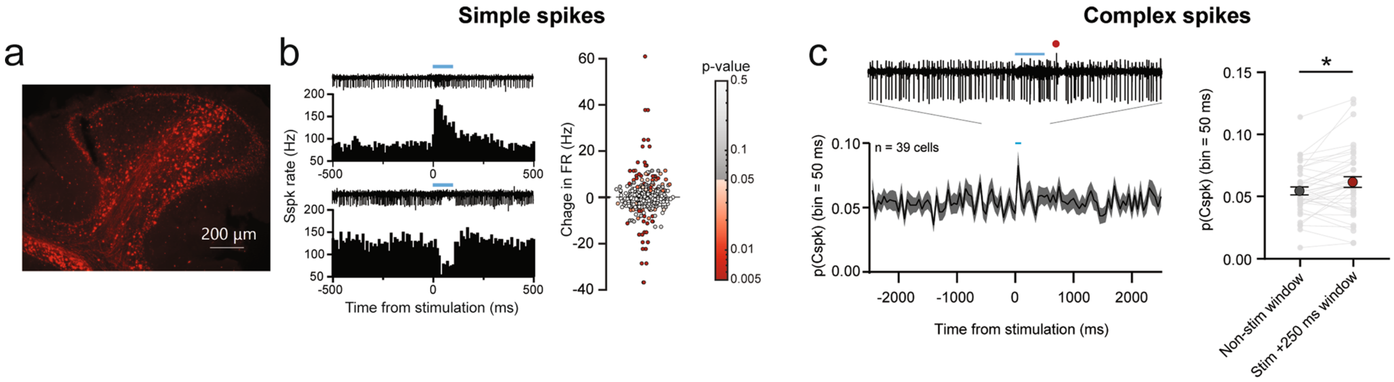

Extended Data Fig. 5 | Changes in PC firing during optogenetic stimulation of mossy fibers. a. Mossy fiber boutons expressing hSyn-ChR2-mCherry in the cerebellar cortex. **b**. Simple spike responses to mossy fiber stimulation. Left: examples of single-cell simple spike responses to mossy fiber stimulation. Right: quantification of simple spike responses to all recorded cells. Significance of differences are indicated by the color and corresponding p-value map. **c**. Cspk responses to mossy fiber stimulation. Left: PSTH of the population of recorded cells with Cspks binned at 50 ms. A single trace showing a Cspk after stimulation is shown above. Right: Quantification of Cspk probability in the 250 ms after stimulation and non-stimulated epochs for each cell. (**p-values:** (**b**) paired t-test, (**c**) 5.6 ×10^{-3}, paired t-test **Sample size:** (**a**) 1 of 4 mice displayed, (**b**) N = 4 animals, 151 cells (**c**) N = 4 animals, 39 cells; * indicates p-value < 0.05; all error bars and bands represent mean ± SEM).

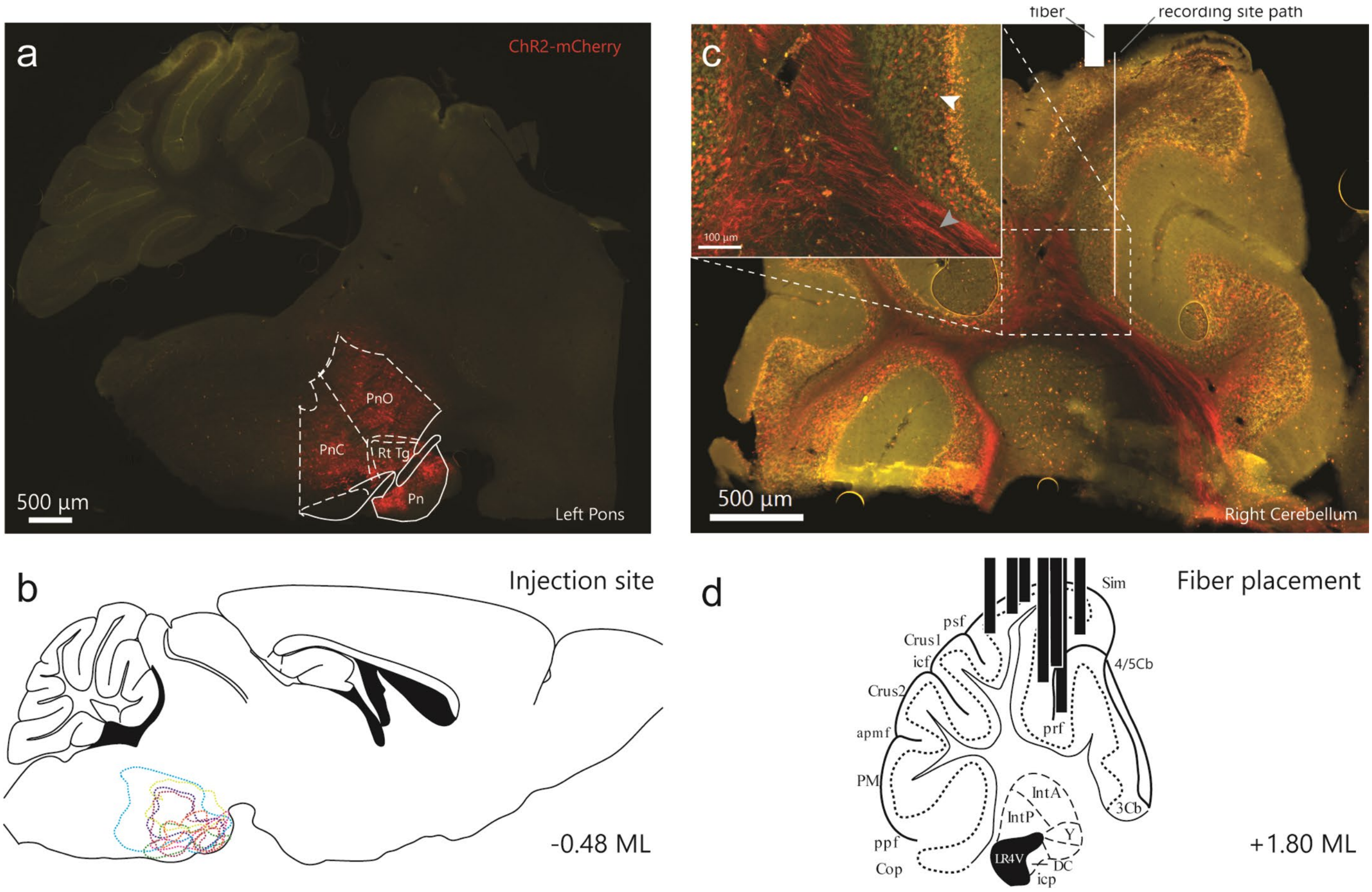

Extended Data Fig. 6 | Opsin expression for mice in behavioral experiments. **a**. Histological section showing ChR2-mCherry expression at the injection site in the left pontine nuclei (Pn: pontine nuclei; RtTg: reticulotegmental nuclei; PnO: pontine reticular nuclei, oral part; PnC: pontine reticular nuclei, caudal part; 1 of 7 mice displayed). **b**. Contours of ChR2 expression in the pontine nuclei for mice used in behavioral experiments. **c**. Right cerebellum of the animal shown in a. Mossy fiber axons (grey arrow) and boutons (white arrow) can be seen expressing ChR2 in the cerebellar cortex. The approximate location of the optical fiber and recording site path are shown in white (1 of 7 mice displayed). **d**. Location of fiber placement in a representative section for animals used in behavioral experiments.

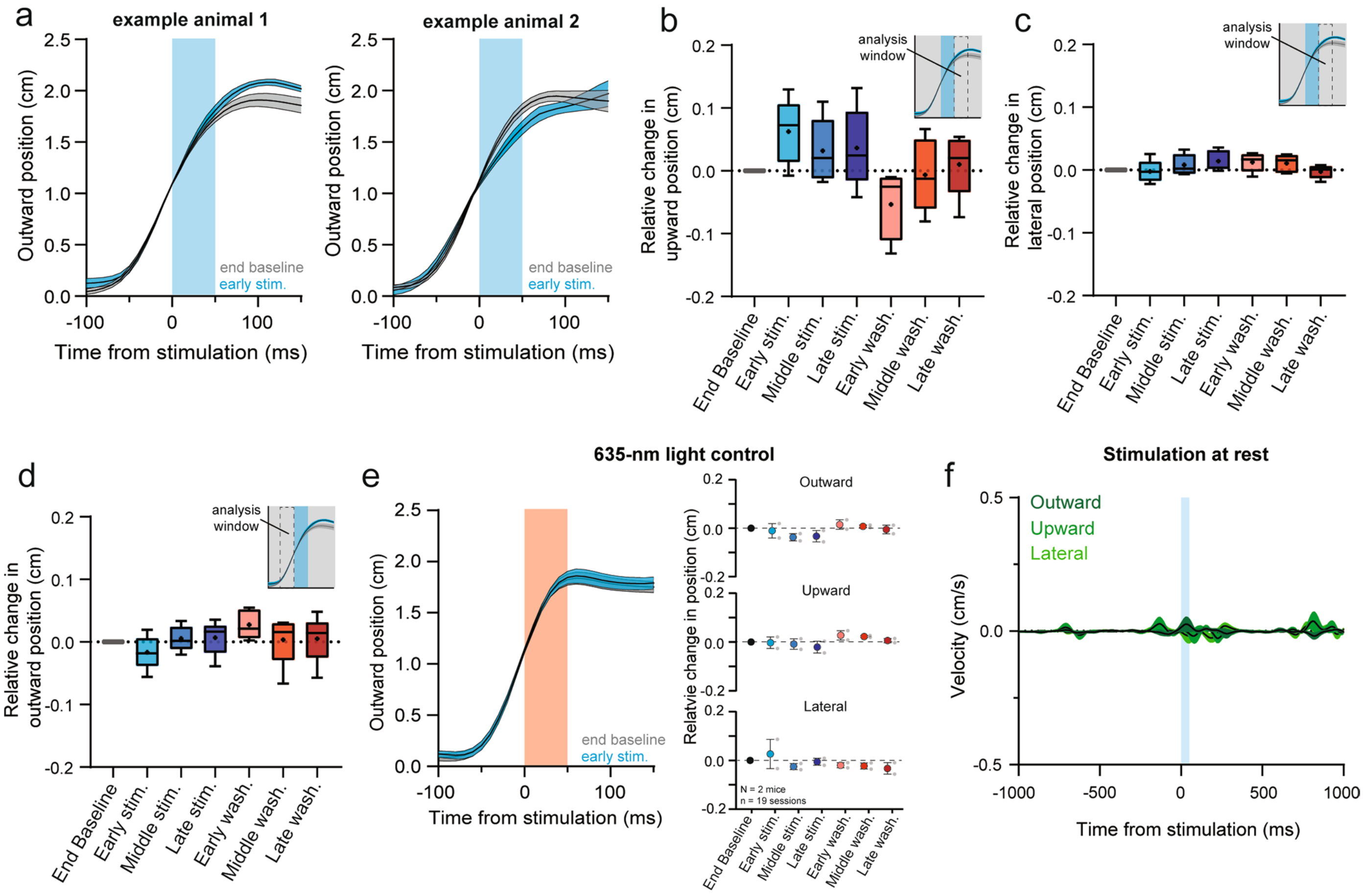

Extended Data Fig. 7 | Fixed-position stimulation supplemental data. **a**. Two example mice with differing effects of stimulation on early reaches in the stimulation block. To account for diverging effects we define the direction of deviation with stimulation as positive and the opposing direction as negative. **b**. Summary of the relative change in upward position for the same data shown in Fig. 3e. Relative change in upward position was assessed in the 50-ms window following the end of stimulation. **c**. Summary of the relative change in lateral position for the same data shown in Fig. 3e. **d**. Summary of the relative change in outward position for in the 50-ms window before stimulation. **e**. Stimulating with 635-nm light did not cause deviations in position or adaptation profiles. **f**. Stimulating while the mouse was awake with its hand at rest on the bar produced virtually no movement. (**Sample size:** (**b-d**) N = 5 mice; 104 sessions, (**e**) N = 2 mice; 19 sessions, (**f**) N = 4 animals, 21 sessions; all error bars and bands represent mean ± SEM; in box and whiskers plots box denotes median and 25th/75th percentiles, whiskers denote 10th and 90th percentiles, circle indicates mean).

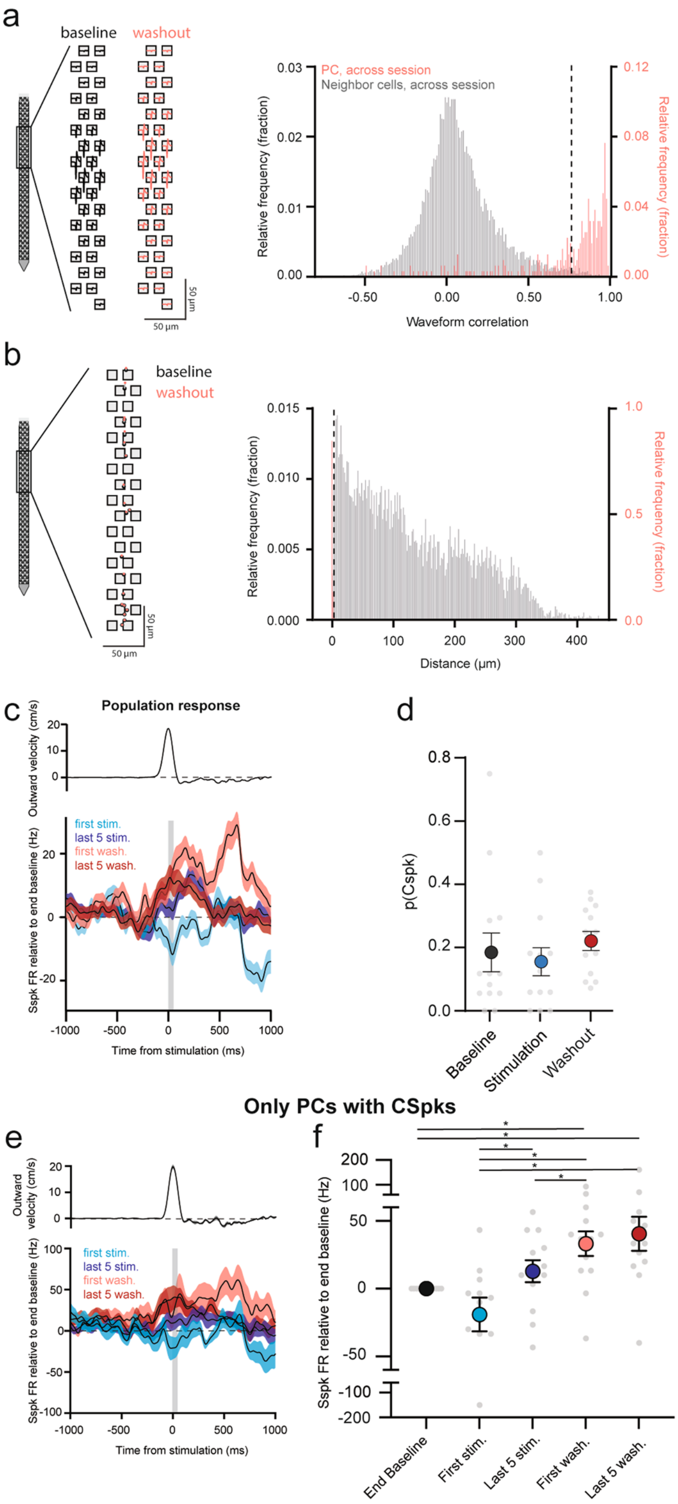

Extended Data Fig. 8 | See next page for caption.

Extended Data Fig. 8 | Assessing unit stability across recording sessions and population responses during fixed-position stimulation experiments. a. Left: Waveforms templates detected on each Neuropixel electrode for a cell during baseline and during washout. Right: Histogram of waveform correlation of PCs across sessions (red) and of mismatched neighboring cells, across the session (shuffled control, grey). PCs with an across-session waveform correlation that fell below the 99th percentile of the shuffled control (dashed line) were excluded from further analysis. **b**. Left: Unit displacement for cells across a session. Baseline unit position is shown in grey and washout position is shown in red. Right: Histogram of unit displacement of PCs across sessions (red) and of mismatched neighboring cells, across the session (shuffled control, grey). PCs with an across-session displacement that fell below the 1st percentile of the shuffled control (dashed line) were excluded from further analysis. **c**. Same as data shown in Fig. 4g with the last 5 stimulated and washout reaches included. The initial stimulation and washout effects are reduced across the stimulation and washout blocks, respectively. **d**. Cspks analyzed during fixed-position stimulation experiments for the baseline, stimulation, and washout blocks. **e**. Same as the analysis shown **a** but only including PCs with Cspks. These cells show similar negative deflections with stimulation then adaptation upwards over the stimulation block compared to the total PC dataset. **f**. Quantification of simple spike firing rates in the stimulation window for the data shown in **c**. (**p-values:** (**f**) 5.1×10^{-5}, RM one-way ANOVA, end baseline vs. first wash: 0.022, end baseline vs. first 5 wash: 0.047, first stim vs. last 5 stim: 0.043, first stim vs. first wash: 6.1×10^{-4}, first stim vs. last 5 wash: 3.8×10^{-3}, last 5 stim vs. first wash: 0.034, Tukey's multiple comparisons test; **Sample size:** (**c**) n = 159 cells (**d-f**) n = 13 cells; * indicates p-value < 0.05; all error bars and bands represent mean ± SEM).

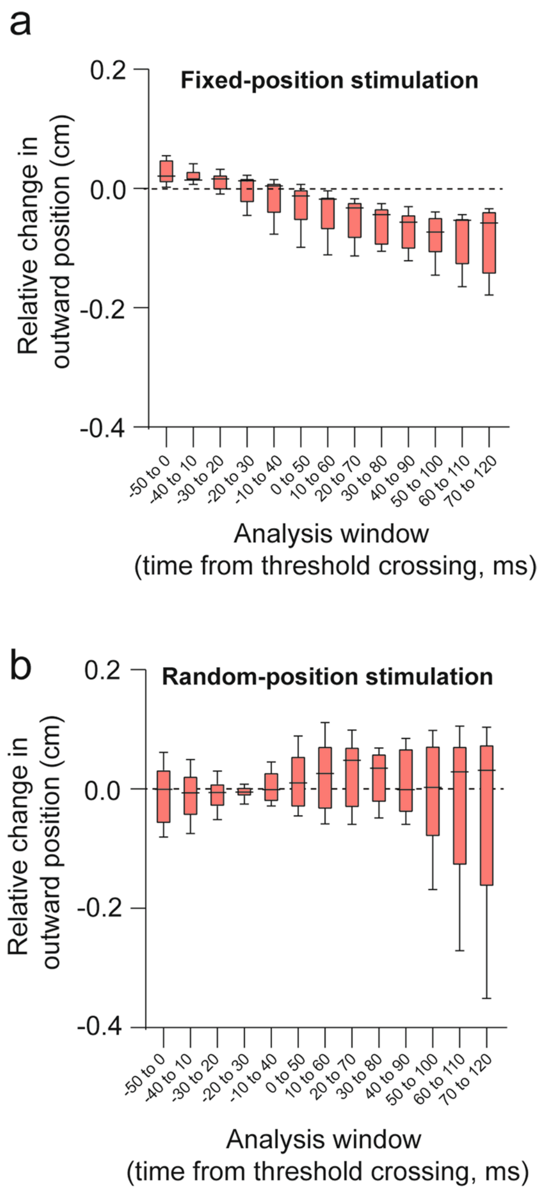

Extended Data Fig. 9 | Temporal analysis of early washout effect for fixed-position and random-stimulation experiments. a. Analysis of fixed-position stimulation experiment early washout reaches in 50-ms time windows across the reach. Each window is shifted 10 ms from the adjacent time window. Aftereffect emerges around the time stimulation was delivered in the stimulation block. **b**. Same as **a** but for random-position stimulation experiments. Consistent aftereffects relative to baseline reaches do not emerge in any of the analyzed windows. (**Sample size:** (**a**) N = 5 mice, 104 sessions, (**b**) N = 5 mice, 60 sessions; in box and whiskers plots box denotes median and 25th/75th percentiles, whiskers denote 10th and 90th percentiles, circle indicates mean).

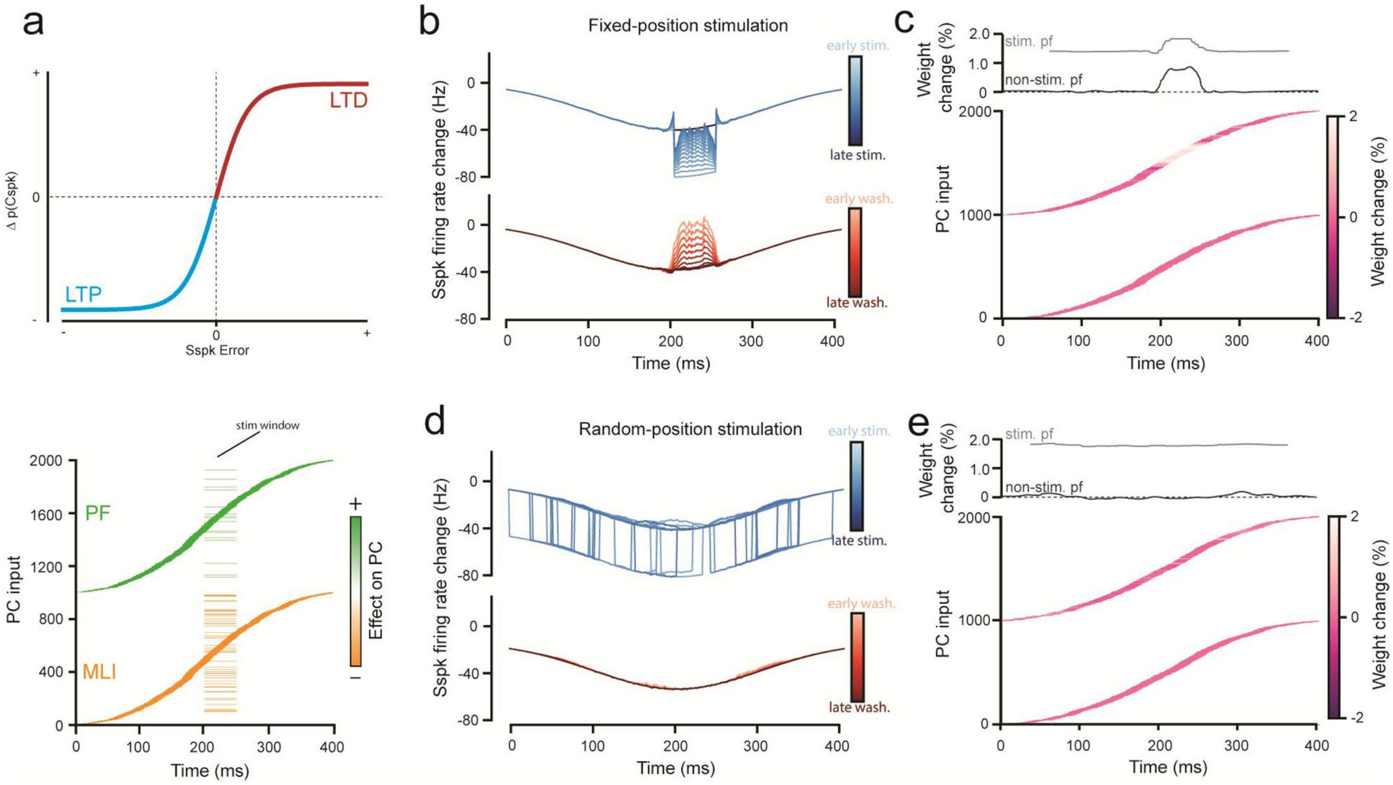

Extended Data Fig. 10 | Cerebellar model adaptation to a negative-going perturbation. a. Model as described in Fig. 6. In this case the number of stimulated MLIs is greater than the number of parallel fibers (bottom) leading to a net negative stimulation effect. Negative simple spike error lowers the probability of Cspks below baseline, leading to LTP (top). **b**. PC simple spike activity during the stimulation block and washout block of fixed-position stimulation as described in Fig. 6b. Here the stimulation reduces firing rate. **c**. Same as described in Fig. 6c. Here parallel fiber weight changes increase to compensate for the stimulation. Note that while not displayed the quantification of the adaptation is identical to the data displayed in Fig. 6d. **d**. Comparison of model output to empirical observations for fixed-position stimulus conditions (Fig. 3). Model closely matches behavioral adaptation. **e**. Same as **b**. but here the stimulation window is randomized across the reach. Note that while not displayed the quantification of the adaptation is identical to the data displayed in Fig. 6d.

nature portfolio

Corresponding author(s): Abigail Person

Last updated by author(s): 4/12/2023

Reporting Summary

Nature Portfolio wishes to improve the reproducibility of the work that we publish. This form provides structure for consistency and transparency in reporting. For further information on Nature Portfolio policies, see our Editorial Policies and the Editorial Policy Checklist.

Statistics

For all statistical analyses, confirm that the following items are present in the figure legend, table legend, main text, or Methods section.

n/a	Confirmed	
☐	☒	The exact sample size (*n*) for each experimental group/condition, given as a discrete number and unit of measurement
☐	☒	A statement on whether measurements were taken from distinct samples or whether the same sample was measured repeatedly
☐	☒	The statistical test(s) used AND whether they are one- or two-sided *Only common tests should be described solely by name; describe more complex techniques in the Methods section.*
☐	☒	A description of all covariates tested
☐	☒	A description of any assumptions or corrections, such as tests of normality and adjustment for multiple comparisons
☐	☒	A full description of the statistical parameters including central tendency (e.g. means) or other basic estimates (e.g. regression coefficient) AND variation (e.g. standard deviation) or associated estimates of uncertainty (e.g. confidence intervals)
☐	☒	For null hypothesis testing, the test statistic (e.g. F, t, r) with confidence intervals, effect sizes, degrees of freedom and P value noted *Give P values as exact values whenever suitable.*
☒	☐	For Bayesian analysis, information on the choice of priors and Markov chain Monte Carlo settings
☒	☐	For hierarchical and complex designs, identification of the appropriate level for tests and full reporting of outcomes
☐	☒	Estimates of effect sizes (e.g. Cohen's *d*, Pearson's *r*), indicating how they were calculated

Our web collection on statistics for biologists contains articles on many of the points above.

Software and code

Policy information about availability of computer code

Data collection	Kinematic data were collected using Motive and Optitrack (version 1.10.3) and streamed in to MATLAB (version 2018a). Electrophysiological recordings were made with Thomas electrodes and Neuropixel probes.
Data analysis	Kinematic data were analyzed in MATLAB using custom written code. Single electrode electrophysiological data were sorted using Psort, Neuropixel data were sorted using Kilosort2 and phy. Sorted electrophysiological data were then analyzed in MATLAB using custom written code.

For manuscripts utilizing custom algorithms or software that are central to the research but not yet described in published literature, software must be made available to editors and reviewers. We strongly encourage code deposition in a community repository (e.g. GitHub). See the Nature Portfolio guidelines for submitting code & software for further information.

Data

Policy information about availability of data

All manuscripts must include a data availability statement. This statement should provide the following information, where applicable:

- Accession codes, unique identifiers, or web links for publicly available datasets
- A description of any restrictions on data availability
- For clinical datasets or third party data, please ensure that the statement adheres to our policy

Data used to make all figures are included as a supplement. Other data in the manuscript are available upon reasonable request to the authors.

Field-specific reporting

Please select the one below that is the best fit for your research. If you are not sure, read the appropriate sections before making your selection.

☒ Life sciences ☐ Behavioural & social sciences ☐ Ecological, evolutionary & environmental sciences

For a reference copy of the document with all sections, see nature.com/documents/nr-reporting-summary-flat.pdf

Life sciences study design

All studies must disclose on these points even when the disclosure is negative.

Sample size	For behavioral experiments an N of 5 animals was used for fixed-position and random-position stimulation experiments, with a minimum of 5 sessions per animal. In red-light control experiments we used 2 animals with repeated sessions for each. Electrophysiological data were taken from multiple animals with >= 10 cells used for each analysis. These values were determined based on previous standards in the literature and were not predetermined with power-analyses. Please see Methods section for a more thorough description of statistical procedures.
Data exclusions	Reaches that where >25% of points were dropped during outreach were excluded from further analysis. For analysis of electrophysiological data during stimulation adaptation experiments, we excluded cells where isolation was unstable across the experiment (described in Methods section).
Replication	Experiments were replicated across animals and sessions. Animal and session replicates are described in the text.
Randomization	Randomization was not feasible due to the nature of the experiments in this study. Specifically, this study does not test, for instance, the efficacy of drug across groups. Rather, within-subject controls were used to determine efficacy and plasticity of stimulation effects. No-across-condition claims are made about descriptive electrophysiological data, so is not applicable.
Blinding	Experimenters were not blinded to the animal identity or experimental condition. This was not done because it was impractical for the type of experiments using electrophysiology and optogenetics and lack of across-group testing. Potential bias was reduced by reporting all outcomes of uniform computer analyses of physiology and behavior.

Reporting for specific materials, systems and methods

We require information from authors about some types of materials, experimental systems and methods used in many studies. Here, indicate whether each material, system or method listed is relevant to your study. If you are not sure if a list item applies to your research, read the appropriate section before selecting a response.

Materials & experimental systems

n/a	Involved in the study	
☒	☐	Antibodies
☒	☐	Eukaryotic cell lines
☒	☐	Palaeontology and archaeology
☐	☒	Animals and other organisms
☒	☐	Human research participants
☒	☐	Clinical data
☒	☐	Dual use research of concern

Methods

n/a	Involved in the study	
☒	☐	ChIP-seq
☒	☐	Flow cytometry
☒	☐	MRI-based neuroimaging

Animals and other organisms

Policy information about studies involving animals; ARRIVE guidelines recommended for reporting animal research

Laboratory animals	Mice were C57BL/6 (19 total: 11 females, 8 males, obtained from Charles River) < 3 months old.
Wild animals	Wild animals were not used.
Field-collected samples	No field-collected material was used.
Ethics oversight	All procedures followed National Institutes of Health Guidelines and were approved by the Institutional Animal Care and Use Committee at the University of Colorado Anschutz Medical Campus.

Note that full information on the approval of the study protocol must also be provided in the manuscript.